LIGO-P080122-00-Z

Results from the first Numerical INJection Analysis (NINJA) project

Benjamin Aylott[1], John G. Baker[2], William D. Boggs[3], Michael Boyle[4], Patrick R. Brady[5], Duncan A. Brown[6], Bernd Brügmann[7], Luisa T. Buchman[4], Alessandra Buonanno[3], Laura Cadonati[8], Jordan Camp[2], Manuela Campanelli[9], Joan Centrella[2], Shourov Chatterji[10,11], Nelson Christensen[12], Tony Chu[4], Peter Diener[13,14], Nils Dorband[15], Zachariah B. Etienne[16], Joshua Faber[9], Stephen Fairhurst[17], Benjamin Farr[17,18], Sebastian Fischetti[8], Gianluca Guidi[10,19], Lisa M. Goggin[5], Mark Hannam[20], Frank Herrmann[21], Ian Hinder[21], Sascha Husa[22,15], Vicky Kalogera[23], Drew Keppel[11], Lawrence E. Kidder[24], Bernard Kelly[2], Badri Krishnan[15], Pablo Laguna[25], Carlos Lousto[9], Ilya Mandel[23], Pedro Marronetti[26], Richard Matzner[30], Sean T. McWilliams[2], Keith Matthews[4], R. Adam Mercer[5], Satyanarayan R. P. Mohapatra[8], Abdul H. Mroué[24], Hiroyuki Nakano[9], Evan Ochsner[3], Yi Pan[3], Larne Pekowsky[6], Harald P. Pfeiffer[4], Denis Pollney[15], Frans Pretorius[27], Vivien Raymond[23], Christian Reisswig[15], Luciano Rezzolla[15], Oliver Rinne[28], Christian Röver[29], Lucía Santamaría[15], Bangalore Sathyaprakash[17], Mark A. Scheel[4], Erik Schnetter[13,14], Jennifer Seiler[15], Stuart L. Shapiro[15], Deirdre Shoemaker[25], Ulrich Sperhake[7], Alexander Stroeer[2], Riccardo Sturani[10,19], Wolfgang Tichy[26], Yuk Tung Liu[16], Marc van der Sluys[23], James R. van Meter[2], Ruslan Vaulin[5], Alberto Vecchio[1], John Veitch[1], Andrea Viceré[10,19], John T. Whelan[9,15], Yosef Zlochower[9]

[1] School of Physics and Astronomy, University of Birmingham, Edgbaston, Birmingham B15 2TT, UK
[2] NASA Goddard Space Flight Center, Greenbelt, MD 20771, USA
[3] Maryland Center for Fundamental Physics, Department of Physics, University of Maryland, College Park, MD 20742, USA
[4] Theoretical Astrophysics 130-33, California Institute of Technology, Pasadena, CA 91125
[5] University of Wisconsin-Milwaukee, P.O. Box 413, Milwaukee, WI 53201, USA
[6] Department of Physics, Syracuse University, Syracuse, New York, 13254
[7] Theoretisch Physikalisches Institut, Friedrich Schiller Universität, 07743 Jena, Germany
[8] Department of Physics, University of Massachusetts, Amherst, MA 01003
[9] Center for Computational Relativity and Gravitation and School of Mathematical Sciences, Rochester Institute of Technology, 85 Lomb Memorial Drive, Rochester, NY 14623

[10] INFN-Sezione Firenze/Urbino, I-50019 Sesto Fiorentino, Italy
[11] LIGO – California Institute of Technology, Pasadena, CA 91125, USA
[12] Physics & Astronomy, Carleton College, Northfield, MN, USA
[13] Center for Computation & Technology, Louisiana State University, Baton Rouge, LA 70803
[14] Department of Physics & Astronomy, Louisiana State University, Baton Rouge, LA 70803
[15] Max-Planck-Institut für Gravitationsphysik, Am Mühlenberg 1 , 14475 Potsdam, Germany.
[16] Department of Physics, University of Illinois at Urbana-Champaign, Urbana, IL 61801
[17] School of Physics and Astronomy, Cardiff University, The Parade, Cardiff, UK
[18] Department of Physics, Rochester Institute of Technology, 84 Lomb Memorial Drive, Rochester, NY 14623
[19] Istituto di Fisica, Università di Urbino, I-61029 Urbino, Italy
[20] Physics Department, University College Cork, Cork, Ireland
[21] Center for Gravitational Wave Physics, The Pennsylvania State University, University Park, PA 16802
[22] Departament de Física, Universitat de les Illes Balears, Palma de Mallorca, Spain
[23] Department of Physics and Astronomy, Northwestern University, Evanston, IL, USA
[24] Center for Radiophysics and Space Research, Cornell University, Ithaca, New York, 14853
[25] Center for Relativistic Astrophysics and School of Physics, Georgia Institute of Technology, Atlanta, GA 30332
[26] Department of Physics, Florida Atlantic University, Boca Raton, FL 33431
[27] Department of Physics, Princeton University, Princeton, NJ 08540
[28] Department of Applied Mathematics and Theoretical Physics, Centre for Mathematical Sciences, Wilberforce Road, Cambridge CB3 0WA, UK, and King's College, Cambridge CB2 1ST, UK
[29] Max-Planck-Institut für Gavitationsphysik, Hannover, Germany
[30] University of Texas at Austun, Austin, Texas, 78712

Abstract. In this paper, we present the results of the NINJA project.

1. Introduction

Binary systems of compact objects, i.e. black holes and neutron stars, are among the most important avenues for testing general relativity and studying its astrophysical implications [1]. The general solution of the binary problem in Newtonian gravity is given by the Keplerian orbits. In general relativity, the Keplerian orbits for a bound system decay due to the emission of gravitational radiation, leading eventually to the merger of the two compact objects and to a single final remnant [2–4]. Since the decay of the orbits is due to the emission of gravitational waves, these waves will carry important information about the dynamics of the binary system. In particular, the waves produced during the merger phase might contain important non-perturbative general relativistic effects potentially observable by gravitational wave detectors. These waves could be detectable by the current generation of gravitational wave detectors such as LIGO and Virgo [5, 6], and detection is very likely with future generations of these detectors.

Two important advances have occurred in recent years which have brought us closer to the goal of observing and interpreting gravitational waves from coalescing compact objects. The first is the successful construction and operation of a world-wide network of large interferometric gravitational wave detectors; these include the three LIGO detectors in the United States, Virgo in Italy, TAMA in Japan [7] and the GEO600 detector in Germany [8]. The TAMA detector was the first interfeometric detector to achieve its design goals, and it collected science data between 1999 and 2003 [7]. The LIGO detectors started collecting science data in 2002 [9], and have now reached their design goals. Between 2006 and 2008, they have collected data at their design sensitivity including more than a year of triple coincident observations; this constitutes the 5th Science run (S5) of the LIGO detectors [10]. The Virgo detector is also close to achieving its design goals and has collected data for a number of months overlapping with the end of the LIGO S5 run [11]. The GEO600 detector has also been operating since 2002 in coincidence with the LIGO instruments, and continuing beyond S5 up to the present time [8]. The LIGO detectors are in the process of being upgraded. The first stage of this upgrade, expected in 2009, is known as "Enhanced LIGO" which will improve the amplitude sensitivity of the detectors by a factor of 2-3. Further upgrades leading to "Advanced LIGO" are expected to be completed by 2014. Upgrades to Virgo leading to a sensitivity comparable to Advanced LIGO are expected on a similar time frame. There are also plans to build second generation cryogenic detectors in Japan known as LCGT. Searching data from these detectors for weak gravitational wave signals over a vast parameter space is a challenging task and significant effort and resources have been invested in it. A number of searches on S5 data for unmodelled bursts and binary coalescences are in progress and a many results, including from previous science runs, have already been reported [12–21].

The other important recent advance has been the impressive success of numerical relativity in successfully simulating the merger phase of Binary Black Hole (BBH) coalescence. The first breakthroughs occurred in 2006 with simulations by Pretorius [22], closely followed by the independent Goddard and Brownsville (now at RIT) results [23, 24]. Since then, a number of numerical relativity groups around the world have successfully evolved various configurations starting from the inspiral phase and going all the way through the merger and to the final remnant black hole. This has lead to important new physical insights in BBH mergers. These include the prediction of large recoil velocities produced by asymmetric emission of gravitational radiation

during the merger process [25–41] and the prediction of the parameters of the remnant parameters for a wide class of initial states [42–53]. Since merger events are also among the most important targets of the gravitational wave detectors mentioned previously, we expect that the detailed information provided by numerical simulations can be used to increase the reach and to quantify the efficacy of data analysis pipelines. However, there are significant challenges to be overcome before numerical relativity results can be fully exploited in data analysis pipelines.

Thus far, most searches for gravitational waves from BBH mergers have relied on post-Newtonian results which are valid when the black holes are sufficiently far apart. Within its range of validity, Post-Newtonian theory provides a convenient analytic description of the expected signals produced by binary systems. The numerical relativity results on the other hand, have not yet been synthesized into an analytic model for the merger phase covering a broad range of parameters, i.e. a wide range of mass ratios, spins and if necessary, eccentricity; there has however been significant progress for the non-spinning case. Similarly, despite significant progress, there is not yet a complete detailed description over the full parameter space of how post-Newtonian and numerical simulations are to be matched with each other. On the data analysis side, many pipelines, especially ones which rely on a detailed model for the signal waveform, have made a number of choices based on post-Newtonian results, and it is important to verify that these choices are sufficiently robust. More generally, it is necessary to quantify the performance of these data analysis pipelines for both detection and parameter estimation. This is critical for setting astrophysical upper limits in case no detection has been made, for following up interesting detection candidates, and of course for interpreting direct detections. Thus far, this has been done using mostly post-Newtonian waveforms, and numerical relativity now provides and important avenue for extending this to the merger phase.

The NINJA project was started in the spring of 2008 with the aim of addressing these issues and furthering close collaboration between numerical relativists and data analysts. NINJA is an open collaboration meant for scientists interested in numerical simulations and gravitational wave data analysis. The first NINJA project considers only BBH simulations. It is expected that future NINJA analyses will be expanded to include, for example, neutron star and supernovae simulations as well.

NINJA is the first project of its kind which attempts to bring to form a close working collaboration between the numerical relativity and data analysis communities. The comparisons and conclusions reported here are thus necessarily limited, and in many cases are only the first steps towards fully understanding the sensitivity of data-analysis pipelines to black hole signals. Nevertheless, we are able to draw the following broad conclusions from this work: First, the current data analysis pipelines used to search LIGO, Virgo and GEO600 data for black hole coalescence are able, at roughly the expected sensitivity levels, to detect numerical waveforms injected into the NINJA data set. Indeed, several of these pipelines are able to detect signals which lie outside the parameter space which they target. This is a non-trivial statement because most detectability estimates to date for these systems have relied on post-Newtonian waveforms which is valid when the black holes are sufficiently far apart. For many of these pipelines, this is the first time they have been tested against numerical waveforms. However, the NINJA data set does not contain non-stationary noise transients, so more work is needed to understand how detection performance is affected by the noise artefacts seen in real gravitational-wave detector data. Second, significant work is required to understand and improve parameter estimation. For instance, none

of the pipelines used in this first NINJA analysis have tried to estimate the spins of the individual black holes, and the estimation of the signal masses by the detection pipelines is poor in most cases. Improvement in this area will be crucial for bridging the gap between gravitational wave observations and astrophysics. NINJA has proven to be extremely valuable at framing the questions which need to be answered. Future NINJA analyses will build upon this work to address these questions.

The rest of this paper is organized as follows: In the next section (2) we will first describe the numerical waveforms that have been contributed, then in Sec. 3 we will describe how the noise NINJA data sets have been generated. The main content of the paper are the descriptions of search methods and results in Sec. 4. The results are grouped by search method into search pipelines using modeled waveforms (4.1), search pipelines using unmodeled waveforms (4.2), a comparison of inspiral-burst-ringdown results (4.3), and Bayesian pipelines (4.4). We conclude with a discussion of our results in Sec. 5.

2. Numerical Waveforms

The NINJA collaboration has studied BBH coalescence waveforms submitted by ten individuals and teams. The collaboration was open to anyone and the only restrictions were that each contribution

- was a numerical solution of the full Einstein equations,
- consisted of only two waveforms, or
- up to five waveforms if they were part of a one-parameter family.

No restrictions were placed on the accuracy of each waveform. All contributions followed the format specified in [54]. The waveforms are plotted in Figures 1 and 2. The contributed waveforms cover a variety of physical and numerical parameters. Most simulations model low-eccentricity inspiral, the mass ratio $q = M_1/M_2$ ranges from 1 to 4, and the simulations cover a range of spin configurations. The initial frequency of the $\ell = m = 2$ mode ranges from $0.033/M$ to $0.203/M$ (where M denotes the sum of the initial black-hole masses). The length of the waveforms varies between a few 100M to over 4000M. The contributions naturally differ in accuracy, both regarding how well they capture the black-hole dynamics and in the extraction of the gravitational-wave signal. Table 1 lists a few key parameters that distinguish the waveforms, and introduces the following tags for the different contributions and codes: `SpEC` for the Cornell/Caltech collaboration code, `UIUC` stands for the University of Illinois at Urbana-Champaign team, PU stands for Princeton University, `MayaKranc` is the Georgia Tech/Penn State code, BAM_HHB and BAM_FAU are contributions using the `BAM` code, `CCATIE` is the AEI/LSU code, `LazEv` is the RIT code, `Lean` is Ulrich Sperhake's code, and `Hahndol` is the Goddard Space Flight Center's code.

The codes listed above use different formulations of the Einstein equations, gauge conditions, mesh structures and more; we will attempt to give a unified presentation of common features first, and then list further details of the approaches separately for each contribution. Full details of each code are given in the references.

The numerical codes follow either of two approaches to solving the Einstein equations: (1) the generalized harmonic formulation, which was the basis of Pretorius's initial breakthrough simulation of coalescing black holes [22], or (2) the moving-puncture approach, following [23, 24]. Both approaches result in canonical choices

for the construction of initial data, the evolution system for the Einstein equations, and the treatment of the singularity inside the black-hole horizons.

Code Ref.	Run	q	$\vec{S}_i/M_i^2$	e	$\omega_{22}\,M$	D/M	eccentricity removal
BAM_HHB	S00 [55]	1	0	< 0.002	0.045	$12\,\hat{y}$	TR-PN [56]
[57, 58]	S25 [59]	1	$0.25\,\hat{z}$	≈ 0.006	0.045	$12\,\hat{y}$	T-PN [34]
	S50 [59]	1	$0.50\,\hat{z}$	≈ 0.006	0.052	$11\,\hat{y}$	– ” –
	S75 [59]	1	$0.75\,\hat{z}$	≈ 0.006	0.06	$10\,\hat{y}$	– ” –
	S85 [59]	1	$0.85\,\hat{z}$	≈ 0.006	0.06	$10\,\hat{y}$	– ” –
BAM_FAU [57, 58]	[52]	1	see caption	qc	0.06	$9.58\,\hat{y}$	T **???**
`CCATIE` [28, 36, 60, 61]	r0 [36]	1	$0.6\,\hat{z}$, $-0.6\,\hat{z}$	qc	0.079	8	TR-PN [56]
	r2 [36]	1	$0.6\,\hat{z}$, $-0.3\,\hat{z}$	qc	0.078	8	– ” –
	r4 [36]	1	$0.6\,\hat{z}$, 0	qc	0.076	8	– ” –
	r6 [36]	1	$0.6\,\hat{z}$, $0.3\,\hat{z}$	qc	0.075	8	– ” –
	s6 [45]	1	$0.6\,\hat{z}$	qc	0.074	8	– ” –
`Hahndol` [63, 64]	kick	3	$0.2\,\hat{x}$, $0.022\,\hat{x}$	qc	0.078	$8.007\,\hat{y}$	T-PN [62]
	non	4	0	qc	0.070	$8.470\,\hat{y}$	– ” –
`LazEv` [23, 65]		1	$0.92\,\hat{z}$	qc	0.07	$8.16\,\hat{x}$	T-PN **ref?**
`Lean` [66]	c	4	0	qc	0.05	$10.93\,\hat{x}$	T-PN [57]
	2	1	$0.926\,\hat{z}$	qc	0.11	$6.02\,\hat{x}$	T-PN [62]
`MayaKranc` [67]	e0 [50]	1	0	qc	0.05	12	TR-PN [56]
	e02 [50]	1	0	0.2	0.05	15.26	n/a
PU [22, 68]	CP [69]	1	$0.063\,\hat{z}$	qc	0.07	$9.5\,\hat{x}$	T-ID [70]
	T52W [71]	1	0	≥ 0.5	0.07		n/a
`SpEC` [72]	q=1 [73, 74]	1	0	$< 10^{-5}$	0.033	$15\,\hat{x}$	TR-it [75]
UIUC [76]	cp [76]	1	0	qc	0.194	$4.790\,\hat{x}$	T-ID [70]
	punc [76]	1	0	qc	0.203	$4.369\,\hat{y}$	T-ID [77]

Table 1. Initial conditions for numerical waveforms. The columns list, in order from left to right, the name of the contribution or code, the name of the run where appropriate, the mass ratio $q = M_1/M_2$ where $M_1 \geq M_2$, the spins of the black holes in vector form (if only one spin is given, both spins are equal), an estimate of the initial eccentricity of the orbit (the entry qc denotes cases where quasicicular inspiral, i.e. zero eccentricity is modeled, but a value of the eccentricity has not been reported), the initial frequency of the $(\ell, m) = (2, 2)$ mode (rounded to three digits), the initial coordinate separation of either the black-hole punctures or the excision surfaces, and where appropriate the method of eccentricity removal. All binaries start out in the xy-plane with initial momenta tangent to the xy-plane. See text for the identification of each contribution, and a description of the notation in the last column. The dimension-less spins of the BAM_FAU run are $(-0.634, -0.223, 0.333)$ and $(-0.517, -0.542, 0.034)$.

2.1. Summary of the simulation algorithms

2.1.1. Initial Data All of the results presented here make the simplifying assumption of conformal flatness for the spatial metric of the initial slice, which leads to some spurious gravitational radiation in the initial data. All contributions attempt to model non-eccentric inspiral, except for the two data sets PU–T52W and `MayaKranc`–

Code	Run	q	ΔT_{100} [sec]	$f_{i,100}$ [Hz]	$M_{30Hz}[M_\odot]$	$\mathcal{M}_{30Hz}[M_\odot]$
BAM_HHB	S00	1	1.03	15	48	21
	S25	1	1.15	15	48	21
	S50	1	1.03	17	56	24
	S75	1	0.81	19	65	28
	S85	1	0.87	19	65	28
BAM_FAU		1	0.54	19	65	28
`CCATIE`	r0	1	0.34	26	85	37
	r2	1	0.37	25	84	37
	r4	1	0.40	25	82	36
	r6	1	0.45	24	81	35
	s6	1	0.59	24	80	35
`Hahndol`	kick	3	0.25	25	84	31
	non	4	0.32	23	75	25
`LazEv`		1	0.43	23	75	33
`Lean`	c	4	0.92	16	54	18
	2	1	0.20	36	118	52
`MayaKranc`	e0	1	1.23	16	54	23
	e02	1	0.74	16	54	23
PU	CP	1	0.29	23	75	33
	T52W	1	0.16	23	75	33
`SpEC`	q=1	1	1.96	11	36	15
UIUC	cp	1	0.10	63	209	91
	punc	1	0.10	66	219	95

Table 2. Characteristic duration, mass and frequencies of the waveforms summarized in table 1. ΔT_{100} and $f_{i,100}$: duration and initial frequency, of waveform when scaled to total mass $M = 100M_\odot$. M_{30Hz}, $\mathcal{M}_{30Hz}$: Total mass and chirp mass, such that the initial frequency is 30Hz (this is the lowest mass for which each waveform was eligible for injection).

e02. However, the degree of "quasi-circularity" varies, and in general one should bear in mind that the definition of eccentricity for fully general-relativistic orbits is not unique. The data set PU–T52W is notable for the fact that the BBH was constructed via scalar field collapse. Specifically, the initial data consists of two, compact, dense distributions of scalar field energy, separated by some distance and Lorentz boosted in opposite directions orthogonal to the line between them. Upon subsequent evolution, each scalar field pulse quickly collapses to form a black hole, with all remnant scalar field energy radiating away from the domain on order of the light-crossing time of the orbit. This is the same time scale on which spurious gravitational radiation present in all current initial data sets leaves the domain of the inspiral, and hence for practical purposes this can be considered a vacuum merger. All other runs start from vacuum initial data.

Most codes (`BAM`, `CCATIE`, `Hahndol`, `LazEv`, `Lean`, `MayaKranc` and the UIUC code) adopt the "moving puncture" approach, following [23, 24]. These codes use puncture initial data [78–80] to model black holes, resulting in initial data that contain a separate asymptotically flat end within each black hole. Constructing such initial data is mathematically well understood [79, 81] and for simple cases the evolution of such initial data has been shown to be equivalent to that of excised black hole [82].

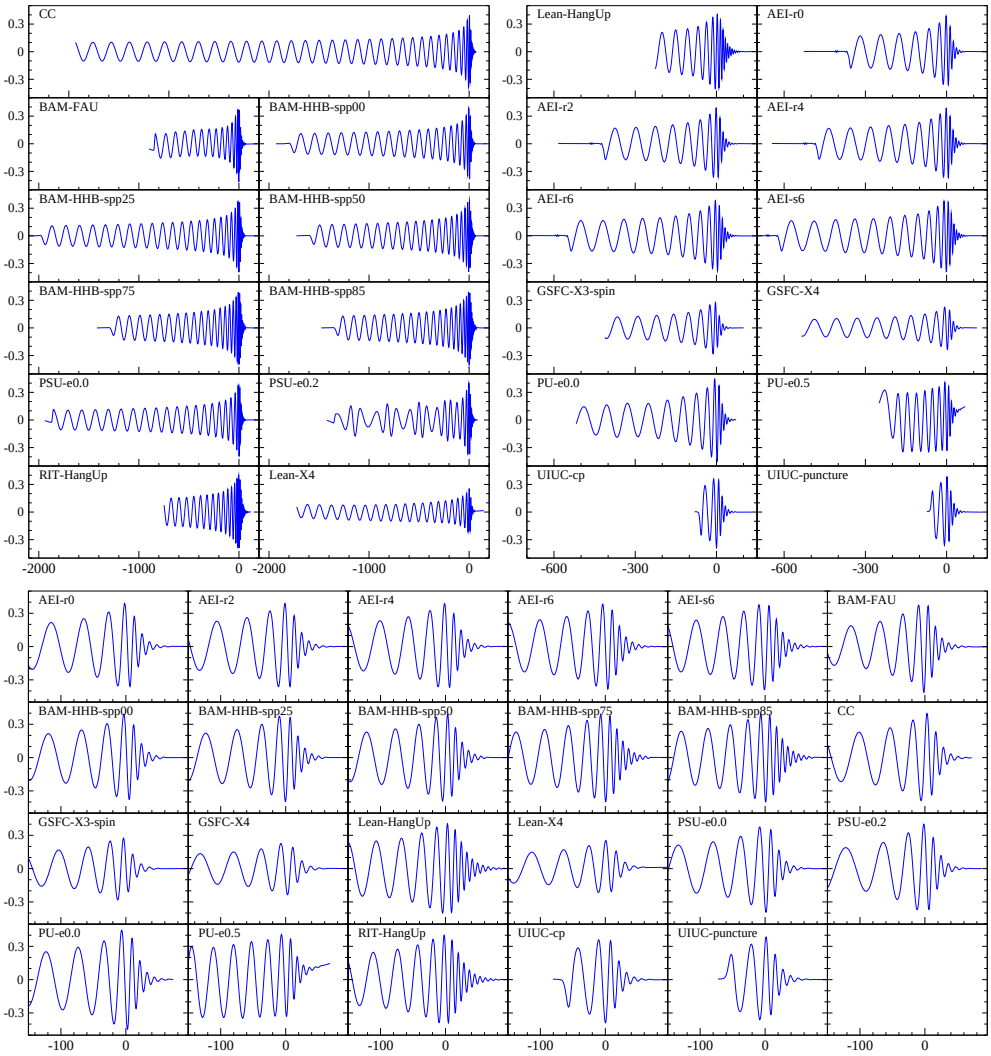

Figure 1. Real part of the $(\ell, m) = (2, 2)$ component of the waveform for all submitted numerical waveforms. The top panels show the complete waveforms: the top-left panel includes waveforms that last more than about $700M$, and the top-right panel includes waveforms shorter than about $700M$. The bottom panel shows an enlargement of the merger phase for all waveforms. The horizontal axis is time in units of M. All waveforms have the same time scaling.

The codes `CCATIE`, `LazEv`, `Lean` and `MayaKranc` all use the same pseudospectral solver for the Einstein constraint equations [83], and `BAM` uses a variant thereof, see [58]. `UIUC-punc` initial data is generated via the LORENE [84] multidomain spectral libraries. The `Hahndol` code uses the second-order-accurate multigrid solver AMRMG [85], which is however tuned to give truncation errors typically much smaller than those produced by the evolution code.

The generalized harmonic codes use conformal thin sandwich initial data [86]. PU-CP and `SpEC` use quasi-equilibrium excision initial data where the interior of the black-

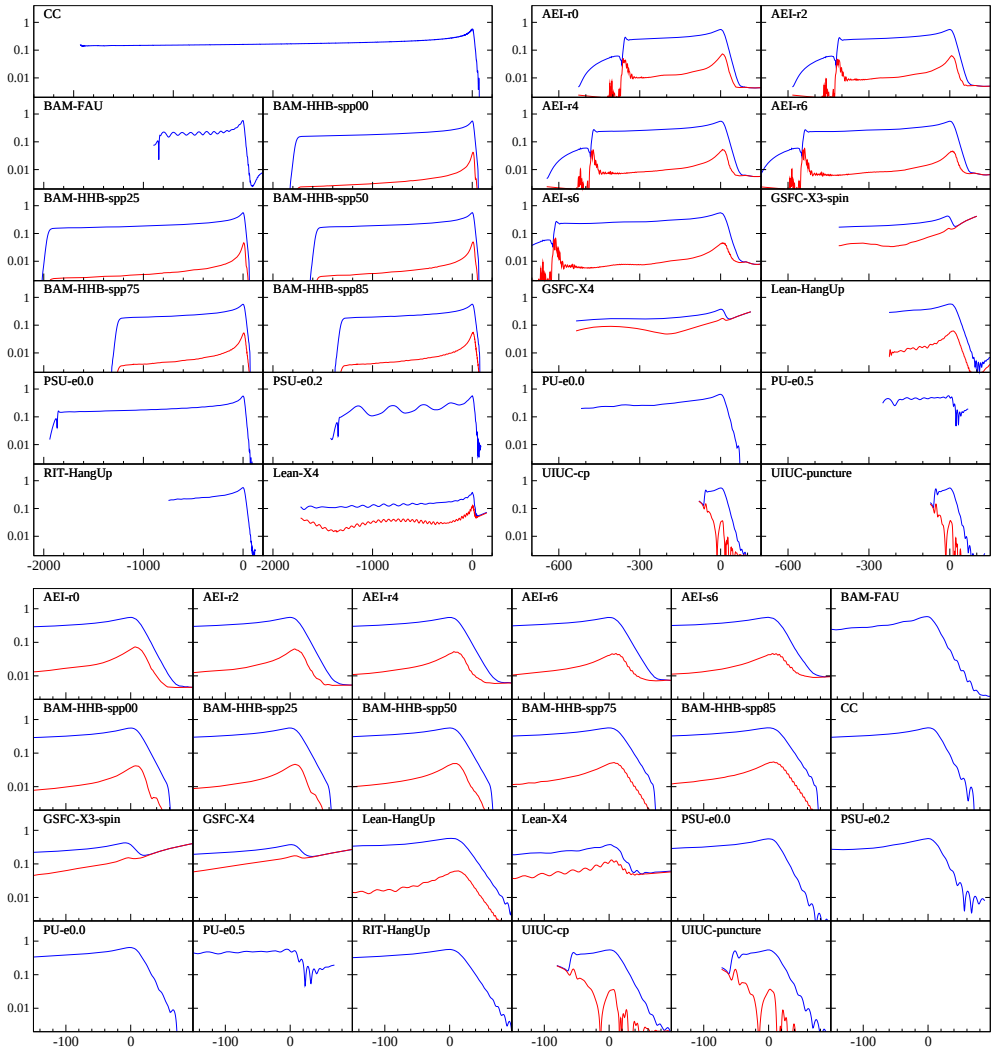

Figure 2. Distribution of power into different spherical harmonics. The blue line shows $\left(\Sigma_{\ell,m}|h_{\ell m}|^2\right)^{1/2}$. A red line, if present, shows the same sum, but *excluding* the $(\ell, m) = (2, \pm 2)$ modes. The red line is always *smaller* than the blue line. The separation between the two lines gives the relative importance of non $(2, \pm 2)$ modes. If no red line is present for a certain run, then only the $(2, \pm 2)$ modes were supplied. The layout is as in Fig. 1: The top panels show the complete waveforms, whereas the bottom panel shows an enlargement of the merger phase.

hole horizons has been excised from the numerical grid. The presence of black holes with desired linear momenta and spins is enforced through the boundary conditions on the excision surfaces and the numerical outer boundary during the solution of the initial-value equations [70, 75, 87]. This "excision technique" is based on the defining property of black holes — the horizons act as causal membranes and information cannot escape from the inside. The `UIUC-cp` simulation uses the same excised initial data, but fills the BH interior with "smooth junk", as described in [76], before evolving with the moving puncture technique. PU–T52W uses initial data in which black holes are formed by scalar field collapse.

All codes take input parameters that ultimately determine the individual black-hole masses M_i, spins $\vec{S}_i$, momenta $\vec{P}_i$ and coordinate separation D of the black holes (one should however be aware that in the strong field regime of general relativity various subtleties are associated with the definition of all of these quantities). In addition, the black-hole masses and dimensionless spins slowly change during the inspiral, which requires additional caution regarding the definition and accuracy of the values of mass, spin, etc. The instantaneous individual black-hole masses can be measured using the *apparent-horizon masses* $M_{i,irr}$, computed from the irreducible mass (given by the area of each hole's horizon) and the spin according to Christodoulou's [88] relation $M_i^2 = M_{i,\mathrm{irr}}^2 + S_i^2/(4M_{i,\mathrm{irr}}^2)$. We generally use the total black-hole mass $M = M_1 + M_2$ to scale dimensionful quantities, although sometimes the total conserved energy (M_{ADM}) is used for this purpose.

Without loss of generality all codes chose the rest frame where $\vec{P}_1 = -\vec{P}_2$ and, thus, the net linear momentum vanishes initially.

Those simulations that attempt to model non-eccentric inspiral use initial parameters calculated by a number of different methods. Ideal initial parameters would produce tangential motion consistent with circular orbits, and radial motion consistent with slow inspiral. The various methods to choose initial parameters can be broadly characterized as those that attempt to provide only tangential motion (so that initially the black holes have no radial momenta), denoted by "T" in the last column of table 3, and those that provide both tangential and radial motion (denoted by "TR"). The procedures to estimate these parameters are based on properties of the initial-data set ("ID"), post-Newtonian methods ("PN"), or an iterative procedure following the results of several trial simulations ("it"). In Table 1 we indicate which of these variants was used, and provide a reference to the specific algorithm; for the post-Newtonian methods in particular there are several variants. Note that the estimates of the resulting eccentricity range from $e \sim 10^{-5}$ (for the `SpEC` contribution) up to $e \sim 0.02$.

The two data sets from the `UIUC` contribution actually compare two *alternative* sets of nonspinning, equal-mass, quasicircular initial data, with initial orbital frequency $M\Omega = 0.0824$: (i) Puncture initial data with coordinate separation $D/M = 4.369$ and initial linear momentum of each BH set according to [77], and (ii) Cook-Pfeiffer initial data with coordinate separation $D/M = 4.790$ [70, 89] (measured from the centroids of the apparent horizons), filling the BH interior with data that smoothly connect to the exterior as described in [76]. Both data sets yield the same final spin $|\vec{S}_{BH}|/M_{BH}^2 = 0.68$, but differ at the level of a few percent in radiated energy and angular momentum.

For the eccentric `MayaKranc` simulation (data set e02), the conservative, 3 post-Newtonian (PN) expressions in Ref. [90] have been used to specify initial data.

These expressions require the specification of the eccentricity e and the mean motion $n = 2\pi/P_r$, where P_r is the radial (pericenter to pericenter) orbital period. There are three PN eccentricities, which are the same to 1 PN order, and we choose e_t, which appears in the PN Kepler equation, following Ref. [90]. The quantity n has been chosen as $n = 0.01625/M$ ($P_r \sim 387M$) and $e = 0.2$. The binary separation, $D/M = 15.264$, was determined from Eq. (23) in Ref. [90], and the tangential linear momentum, P/M=0.0498, of each black hole at apocenter was obtained from $J = PD$, where J is the total angular momentum computed as a post-Newtonian expansion in n and e (Eq. (21) in Ref. [90]).

2.1.2. Evolution systems There is a long history of casting the Einstein equations into systems of partial differential equations, and in particular into the form of a well-posed initial value problem. The process of writing the covariant Einstein equations in the form of three-dimensional tensor quantities that evolve in time is commonly referred to as a 3+1 split. The core idea here is to choose coordinates $\{x^i, t\}$ $(i = 1, 2, 3)$ such that the spacetime metric can be written in the form

$$ds^2 = -(\alpha^2 - \gamma_{ij}\beta^i\beta^j)dt^2 + 2\gamma_{ij}\beta^j dt\, dx^i + \gamma_{ij}dx^i\, dx^j, \qquad (1)$$

where γ_{ij} is a positive-definite metric on the slices of constant time t, and the scalar function α and vector field β^i are commonly used to encode the freedom of coordinate choice. They may in principle be freely specified, and in practice are judiciously prescribed through further evolution equations.

Code	System	Technique	shift	$M\eta$	r_{max}/M	r_{ext}/M	$\frac{h_{min}}{0.001M}$
BAM_HHB	BSSN	FD–6	000	2	773	90	56, 19
BAM_FAU	BSSN	FD–6	000	2	436		16
CCATIE	BSSN	FD–4	000	1	819	160	20
Hahndol	BSSN	FD–6	000	2	> 1000	45	19, 13
LazEv	BSSN	FD–4	ttt	6		40	3.1
Lean	BSSN	FD–4, 6	000			60, 61	19, 13
MayaKranc	BSSN	FD–6	000			70	16, 19
PU	GH	FD–2	n/a	n/a	∞	50	
SpEC	GH	Spectral	n/a	n/a	$450 \to 230$	$75 - 225$	~ 3
UIUC	BSSN	FD–4	000	0.25	409.6	70	25

Table 3. Some properties of the NR evolution codes. The columns list, for each contribution, the employed evolution system, the numerical technique (FD-k stands for finite differences using k-th order stencils in the bulk), the time derivative and η choices for the $\tilde{\Gamma}$-driver shift, the approximate location of the outer boundary, the radii used for wave extraction, and the finest grid–spacing. If two numbers are given they correspond to the two runs of the respective code listed in table 1 (for BAM_HBB, $h_{\rm min} = 0.019M$ applies to all runs with spin). For the SpEC run, $r_{\rm max}$ decreases during the run and the waveform is extrapolated to $r_{\rm ext} = \infty$ based on extraction at radii in the given interval [73, 74].

The contributions presented here use versions of either of the two formulations for which successful multi-orbit evolutions of black-hole binaries have been published so far, the generalized harmonic and the BSSN/moving-puncture formulation of the Einstein equations. For overviews of writing the covariant Einstein equations as a time evolution problem, see e.g. [91–93].

The generalized harmonic formulation (see e.g. [93]) writes the evolution equations in manifestly hyperbolic form as a set of generalized wave equations for the space–time metric $g_{\mu\nu}$. The `SpEC` code uses this formulation in first order form [94], while the PU contribution is based on a second differential order version of the equations. Gauge conditions are enforced by specification of gauge-source functions H^μ, either as a specified function of time, or through evolution equations [22, 73, 74, 95].

All other codes use the first order in time, second order in space BSSN formulation of the Einstein evolution equations [96–98] in combination with hyperbolic evolution equations for the lapse and shift. The BSSN formulation consists of making a conformal decomposition of the spatial metric, $\gamma_{ij} = \psi^4 \tilde{\gamma}_{ij}$, and all other variables, and the introduction of $\tilde{\Gamma}^i = \partial_j \tilde{\gamma}^{ij}$, which is treated as an independent variable. The moving-puncture treatment of the BSSN system involves evolving not the conformal factor ψ but either $\phi = \ln \psi$ (`CCATIE`) or $\chi = \psi^{-4}$ (all other BSSN codes); it also consists of the gauge choices that we will summarize below.

All BSSN-based contributions evolve the lapse according to the 1+log slicing condition [99],

$$(\partial_t - \beta^i \partial_i)\alpha = -2\alpha K\,. \tag{2}$$

The shift vector field β^i is evolved according to variants of the $\tilde{\Gamma}$-driver condition [61, 64]). During the evolution these gauge conditions change the geometry of the "puncture singularity" and soften the singularity as discussed in [100–102].

The original $\tilde{\Gamma}$-driver condition introduced in [61] is

$$\partial_t \beta^i = \frac{3}{4} B^i, \quad \partial_t B^i = \partial_t \tilde{\Gamma}^i - \eta B^i. \tag{3}$$

The factor of 3/4 is chosen such that at large distances the propagation speed of the hyperbolic equation (3) equals the coordinate speed of light [61], and the quantity η is a parameter with the dimensions of the inverse of a mass and has the effect of compensating for coordinate drifts: larger values of η lead to a stronger initial growth of the apparent horizon, and thus to a magnification effect for the black holes [57]. Variants of this condition [23, 24, 64, 103, 104] consist of replacing some or all of the ∂_t derivatives with $\partial_0 = \partial_t - \beta^i \partial_i$. We will label these options with reference to each of the three time derivatives in (3): "ttt" denotes that ∂_t is used for all three derivatives, "000" denotes usage of ∂_0. The properties of the different choices are studied in [64, 104], and in [104] it is proven that the combination of the BSSN equations with the "1+log" slicing condition (2) and the "000" shift choice yields a well-posed initial-value problem.

Small differences in the evolutions also originate in the choice of initial lapse (all BSSN codes initialize the shift quantities β^i and B^i to zero). We first define a Brill-Lindquist-like conformal factor, $\psi_{BL} = 1 + \frac{M}{4r_1} + \frac{M}{4r_2}$, where r_A is the distance to the Ath puncture, and we recall that M is the total black-hole mass of the binary system. The RIT contributions choose $\alpha(t = 0) = 2/(1 + \psi_{BL}^4)$. BAM_HHB, `MayaKranc` and the UIUC group use $\alpha(t = 0) = \psi_{BL}^{-2}$, and BAM_FAU choose $\alpha(t = 0) = [(\psi_{BL} - 1)/2 + 1]^{-4}$. **Others?**

The generalized harmonic codes (PU and `SpEC`) employ black-hole excision, i.e. they excise from the computational grid a region around the singularities inside each black hole.

2.1.3. Radiation Extraction All groups use one of two popular methods to estimate the gravitational-wave signal at a finite distance from the source: The `SpEC` and `CCATIE` contributions use the Zerilli-Moncrief perturbative formalism [105–107] (with `SpEC` following a version restricted to a Minkowski background in standard coordinates [108]), all other contributions use the Newman-Penrose curvature scalar ψ_4; (the `CCATIE` code implements both methods for the calculation of the waveforms and has shown that very similars results are obtained when using either approach [28, 36]); summaries and details on the implementations within particular codes can be found, for instancem in refs. [36, 57, 66, 109] [MORE REFS]. Since the gravitational-wave signal can only be defined unambiguously at null infinity, one typically considers several extraction radii and performs some form of convergence test, although for the present purpose most groups only report results for a single extraction radius. At finite radius both methods depend on the coordinate gauge, and the Newman-Penrose method additionally requires the choice of a tetrad, which is obtained by Gram-Schmidt orthonormalization of a tetrad of coordinate vectors.

For this work, all waveforms have been contributed as spherical harmonic modes of spin-weight -2 of the strain, according to the specification in [54]. Computation of the strain from the Zerilli-Moncrief odd- and even-parity ($Q^{\times}_{lm}$, Q^{+}_{lm}) multipoles of the metric perturbation requires one time integration [36, 106, 107], computation of the strain from the Newman-Penrose curvature scalar ψ_4 requires two time integrations. This requires the proper choice of the constants of integration, and may require further "cleaning procedures" to get rid of artefacts resulting from the finite extraction radii. For example, for the BAM_HHB contribution unphysical linear drifts were removed by a variant of the method described in [110], where higher order than linear polynomials were used to remove unphysical drifts from higher modes to further improve the properties of the derived strain. In the RIT contribution, the strain was computed by taking the Fourier transform of ψ_4, removing modes in a small region around $\omega = 0$, then dividing by $-\omega^2$ and taking the inverse Fourier transform.

2.1.4. Numerical Methods and Computational Infrastructure There are large overlaps regarding the numerical methods in the present waveform contributions. With the exception of the `SpEC` code, which uses a multi-domain pseudospectral method, all codes use finite-difference methods to discretize the equations. With the exception of the PU contribution, which uses a second-order-accurate implicit evolution scheme, all other codes use an explicit algorithm based on method of lines: Usually standard fourth-order-accurate Runge-Kutta time stepping, except for the `SpEC` code which uses a fifth order Cash–Karp time-stepper with adaptive step–size.

The moving-puncture/BSSN based codes use standard centered finite differencing stencils, however the terms corresponding to the Lie-derivative with respect to the shift vector are off-centered (upwinded) by one grid-point. The `CCATIE`, RIT and UIUC codes use fourth-order-accurate stencils, the `BAM`, and `MayaKranc` codes use sixth-order stencils, the `Hahndol` code uses sixth-order stencils combined with fifth-order upwinded stencils [111], and the `Lean` code uses fourth-order for equal-mass and sixth-order for unequal-mass data sets. All of these codes add standard fifth-order Kreiss-Oliger dissipation [112, 113] to the right-hand-sides of the evolution equations. The finite-difference orders described here apply to the bulk of the computational domain. There are contributions at other orders in different parts of the codes, which we will describe below. However, the finite-difference order in the bulk plays the dominant role in defining the accuracy of the present simulations (and indeed the

spatial finite-differencing order seems to dominate over the order of time integration when sufficiently small timesteps are used), and for that reason we denote the finite-difference order of each code in Table 3 with the bulk spatial finite-difference order.

All codes except the `SpEC` code use variants of Berger-Oliger mesh-refinement. The PU and `Hahndol` codes employ full adaptive mesh refinement, while the other codes use a hierarchy of fixed refinement boxes which follow the motion of the black holes. Several of the codes are based on the `Cactus` computational toolkit [114, 115] and the `Carpet` mesh-refinement code [116, 117] (`CCATIE`, `Lean`, `MayaKranc`, RIT, UIUC). The BAM_HHB and BAM_FAU contributions both use the `BAM` mesh refinement code, and the `Hahndol` code uses the `PARAMESH` infrastructure [118].

The `Hahndol` code uses a uniform time step, all other mesh refinement codes use variants of Berger-Oliger mesh-refinement with a time step that depends on the grid spacing, and for these codes time interpolation at mesh-refinement boundaries introduces second-order errors.

For interpolation between meshes of different spacing, the groups that used fourth- or higher order methods all use fifth order (`CCATIE`, UIUC,`MayaKranc`) or sixth-order accurate (`BAM`, **Others?**) polynomial interpolation in space between different refinement levels so that all spatial operations of the AMR method (i.e. restriction and prolongation) are sixth-order accurate and the second derivatives of interpolated values are at least fourth-order accurate.

A proper numerical treatment of gravitational waves in asymptotically flat spacetimes wave would include null infinity and not require boundary conditions at some finite distance from the source. All codes circumvent this problem in essentially heuristic ways. The PU code uses spatial compactification combined with numerical dissipation, all BSSN codes use heuristic outgoing wave boundary conditions (which will in general violate constraint preservation and potentially well-posedness and will result in reflections of the outgoing radiation,). The `SpEC` code, in contrast, uses constraint-preserving outer boundary conditions which are nearly transparent to outgoing gravitational radiation and gauge modes [119].

Note that several of the groups use the same apparent horizon finder code (AHFinderDirect) [120] (`Hahndol`, UIUC, `CCATIE`, `LazEv`, `MayaKranc`, `Lean`).

2.2. Accuracy

Estimates on accuracy are reported for the BAM_HHB and `SpEC` contributions. For the BAM_HHB simulations reasonably clean sixth-order convergence was observed, as reported in [55, 59]. In the waveform $r\Psi_4$, extracted at $R_{ex} = 90M$, the uncertainty due to numerical errors and the use of finite extraction radii is estimated as 0.25 radians in the phase and less than 3% in the amplitude of the $l = 2, m = 2$ mode. Modes up to $l = 8$ were calculated; the phase uncertainty is the same for all of them, but we estimate that the amplitude uncertainty increases to as much as 10% for the highest modes.

The `SpEC` contribution is the only one that extrapolates the gravitational wave signal to infinite extraction radius (using third-order polynomial extrapolation [73]). Various convergence tests indicate that the resulting extrapolated waveform is accurate to 0.02 radians in phase and 0.5 percent in amplitude.

3. The NINJA data

The data provided by the numerical relativity groups follows the format outlined in [54]. The format is based on the mode decomposition of the gravitational radiation field at large distances from the source. Let us start with the gravitational waveform $h_{\mu\nu}$. In the Transverse-Traceless (TT) gauge, we only need the spatial components h_{ij}, and we assume that we are sufficiently far away from the source so that the $1/r$ piece dominates:

$$h_{ij} = A_{ij}\frac{M}{r} + \mathcal{O}\left(r^{-2}\right) , \tag{4}$$

where M is the total mass of the system, r is the distance from the source, and A_{ij} is a time dependent TT tensor. In the TT gauge, h_{ij} has two independent polarizations denoted h_+ and $h_\times$ [54]. As usual, the complex function $h_+ - ih_\times$ is decomposed into modes using spin weighted spherical harmonics ${}^{-2}Y_{lm}$ of weight -2:

$$h_+ - ih_\times = \frac{M}{r}\sum_{\ell=2}^{\infty}\sum_{m=-\ell}^{\ell} H_{\ell m}(t)\,{}^{-2}Y_{\ell m}(\iota,\phi)\,. \tag{5}$$

The expansion parameters H_{lm} are complex functions of the retarded time $t - r$ and, if we fix r to be the radius of the sphere at which we extract waves, then H_{lm} are functions of t only. The angles ι and ϕ are the azimuthal and polar angles in a suitable coordinate system centered on the source. The numerical relativity groups are required to provide one ASCII data file for each mode (ℓ, m) that contributes appreciably to the final waveform. Each data file consists of three columns: time in units of the total mass, and the real and imaginary parts of the mode coefficients $H_{\ell m}$ as a function of time. Note that the total mass M scales both the time and the amplitude; thus the waveform for each simulation can in principle be scaled to an arbitrary value of the mass (this generally changes in the presence of matter fields, say for neutron stars or supernovas).

To produce the signal as seen by a gravitational wave detector, we need to go from this mode decomposition to the strain $h(t)$ produced by a source with particular values of the total mass, orientation and distance in a particular detector. Given the $H_{\ell m}$, the total mass, the distance to the source, and the angles (ι, ϕ), we calculate $h_{+,\times}$ using Eq. (5), and use the detector response functions $F_{+,\times}$ to get the observed strain

$$h(t) = h_+(t)F_+(\Theta,\Phi,\psi) + h_\times(t)F_\times(\Theta,\Phi,\psi)\,. \tag{6}$$

Here (Θ, Φ) are sky-angles in the detector frame and ψ is the polarization angle, the time t should be in seconds, and we choose a sampling rate of 4096 Hz, a value commonly used in LIGO/Virgo inspiral searches that assures a tolerable loss in signal-to-noise ratio due to the discrete time steps. The procedure for generating the NINJA data-set is to first generate a random population of binary black hole systems, then generate signals corresponding to this population and at the appropriate sampling rate, and add the signals to stationary Gaussian noise colored with the initial LIGO and Virgo design power spectral densities. The software for carrying out this procedure is freely available as part of the LIGO Algorithms Library [121].

The population of signals from the numerical relativity data was obtained in the following manner. We generate random values for the total mass, distance and orientation. The logarithm of the distance is drawn from a uniform distribution ranging from 50 Mpc to 500 Mpc, and the orientations and masses are chosen from

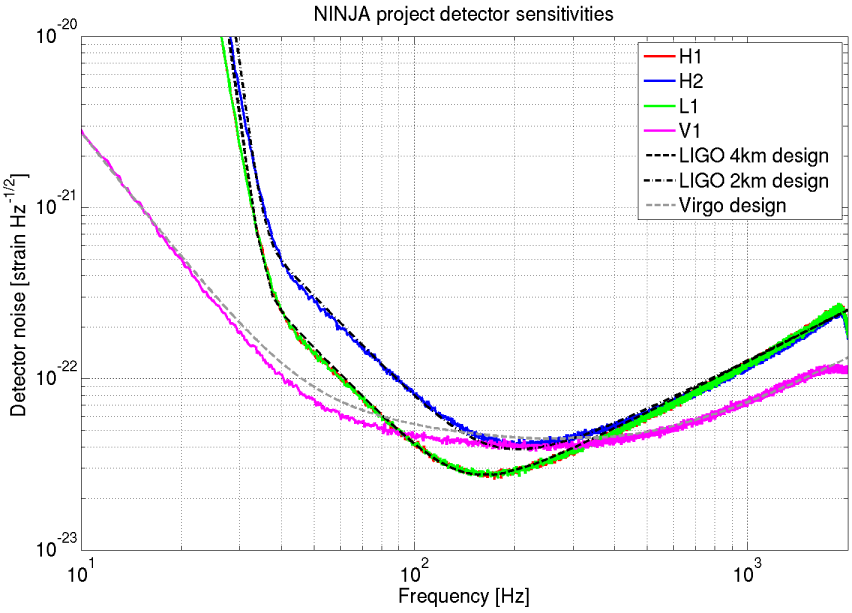

Figure 3. The NINJA data noise curves and the design spectra of the first generation LIGO and Virgo detectors.

a uniform distribution within a mass range of $20M_\odot \leq M \leq 350M_\odot$ [double-check and add range of individual masses?]. We also require that the starting frequency of the dominant $\ell = m = 2$ mode of the signal is not more than 30 Hz, an appropriate threshold given the sensitivity curve of the LIGO and Virgo initial detectors. In practice this sets a lower limit on the value of M that a particular waveform can be scaled by; the longer the waveform, the lower the value of M it can be injected at. To get a good sample of long injected waveforms, we systematicaly choose a lower range of masses for the longer waveforms which had smaller values of f_{22} in Table 1. The final signal is required to have a signal-to-noise ratio (SNR) between 5 and 30 in all the interferometers. No restrictions were placed on the other simulation parameters, i.e. the spins, mass-ratios and eccentricities. Similarly, for this first NINJA data-set, there was no explicit requirement of the waveform accuracy or the waveform extraction methods; these choices were left to the numerical relativity groups.

The noise curves for the data and the design noise curves for the LIGO and Virgo detectors are shown in Fig. 3. We ensure that waveforms from all the participating groups are equitably represented by generating approximately 12 signals from the waveforms supplied by each group. The time interval betwen adjacent injected signals is chosen to be a random number between 700 ± 100 sec. In the end, the NINJA data set consisted of a total of 126 signals injected in a total of 106 segments each 1024 sec long, thus spanning a duration of a little over 30 hours.

4. Data Analysis Results

Analysis of the NINJA data was open to all and nine groups submitted contributions using a variety of analysis techniques. Participating groups were provided with the

NINJA data set containing signals embedded in noise, as described in the last section, and the parameters of the injected signals. Analysts were not given access to the raw numerical relativity data or noiseless injection data.

Methods used to analyze the NINJA data include: matched-filter based searches, un-modeled waveform searches using excess-power techniques, and Bayesian model and parameter estimation techniques. Where possible, the performance of different searches is compared; however, the limited scope of the NINJA data set makes detailed comparisons difficult. We plan to address this in future NINJA analyses. A list of the data analysis contributions is shown in Table 4.

Group	Analysis
AEI	Phenomenological Waveforms in CBC pipeline
Birmingham	Bayesian Model Selection
Cardiff	Post-Newtonian (PN) Templates in CBC pipeline
Cardiff, Maryland	EOBNR waveforms in CBC pipeline
Goddard	Hilbert Huang Transform
Northwestern	Markov Chain Monte Carlo
Syracuse	Extended η PN Templates in CBC pipeline
UMass, Urbino	Q-pipeline analysis
UWM	PN templates in CBC pipeline, Neyman-Pearson criteria
UWM, UMass, Urbino	Ringdown analysis
UWM, UMass, Urbino	Inspiral, Merger, Ringdown combined search

Table 4. The data analysis contributions to the NINJA project.

This section presents the results of the NINJA analysis. Sections 4.1 and 4.2 describe results of analyses using modeled (matched-filter) and un-modeled waveforms, respectively. Comparisons between these analyses are given in Section 4.3 and Section 4.4 presents the results of Bayesian model selection and parameter estimation analyses.

4.1. Search pipelines using modeled waveforms

When the waveform of the target signal is known, matched filtering is the optimal search technique for recovering signals buried in stationary noise [122, 123]. This section describes the results of filtering the NINJA data with matched-filter based analysis pipelines. Results are given for waveforms that span only the inspiral signal, the ringdown alone, and the full inspiral, merger and ringdown. Although the morphologies of these waveforms differ, the underlying analysis techniques are similar in all cases. All the contributions in this section use a pipeline developed by the LIGO Scientific Collaboration (LSC) and Virgo Collaboration to search for gravitational waves from binary neutron stars and black holes in a network of detectors [15, 124]. We first describe the features of this pipeline common to all the contributed matched-filter analyses before presenting the results of searching the NINJA data using different matched-filter templates.

The LSC-Virgo search pipeline performs a series of hierarchical operations in order to search for real signals buried in the detector noise: Given a desired search parameter space and waveform model, a "bank" of templates is created to cover the parameter space such that the fractional loss in signal-to-noise ratio (SNR) between

any signal and the nearest template is less than a specified value (typically 3%). All the NINJA inspiral searches use a non-spinning template bank parameterized by the two component masses of the binary [125–127]. It has been found that searches for spinning binaries using waveforms which neglect the effect of spin are reasonaly effective in most cases [124]. Ringdown searches use a two parameter template bank parameterized by the frequency and quality factor of the signal constructed to cover the desired range of mass and spin [128]. Data from each of the detectors is separately match filtered against this bank of waveforms [128, 129] and a "trigger" is produced whenever the SNR exceeds the desired threshold. All the analyses used a threshold of 5.5. A test is then performed which discards triggers which do not have coincident parameters in two or more detectors (time and masses for inspiral searches, and time, mass and spin for ringdown searches) [130, 131]. These coincident triggers provide the gravitational-wave candidates for the ringdown analysis. The triggers are ranked by a detection statistic ρ_c constructed from the SNRs of the $N \geq 2$ individual triggers in a coincidence by $\rho_c = (\sum_{i=1}^{N} \rho_i^2)^{1/2}$. Coincident inspiral triggers are subject to a second stage of filtering in which "signal-based vetoes" are also calculated, which aim to separate true signals from noise fluctuations [132, 133]. Signal-based vetoes could also be employed for ringdown searches, but at present they are not implemented in the pipeline. For each trigger, we construct an effective SNR $\rho_{\rm eff}$, which combines the matched filter SNR and the value of the χ^2 signal-based veto [132]. This has been found to be more effective at distinguishing signals from non-stationary noise transients than SNR alone [15, 124]. A second test is then performed to discard coincidences in which signal-based vetoes reduce the number of triggers to less than two. These coincidences provide the candidate gravitational wave signals for the inspiral-based pipelines and they are ranked by the combined effective SNR $\rho_{\rm eff} = (\sum_{i=1}^{N} \rho_{{\rm eff}\ i}^2)^{1/2}$. To evaluate the sensitivity of the analyses, we compare the list of gravitational-wave candidates and the parameters of the numerical relativity signals injected into the NINJA data.

Six groups contributed matched filter results to this analysis and the results can be roughly divided into three categories based on the waveform templates used: (i) searches based on the stationary-phase approximation to the inspiral signal, which are designed to capture various stages of the inspiral, merger and ringdown, (ii) searches which use waveforms designed to model the full inspiral-merger-rindown signal, (iii) searches using ringdown-only waveforms obtained from black hole perturbation theory. Within these categories, different parameter choices were made in order to investigate the ability of the pipeline to detect the numerical relativity simulations. Each of these three approaches is described independently in the following sections. A comparison between these results is given in Section 4.3.

4.1.1. Stationary Phase Inspiral Templates The workhorse template of the LSC-Virgo search pipeline is based on the stationary phase approximation to the Fourier transform of the non-spinning post-Newtonian inspiral [129, 134]. This waveform (refered to as SPA or TaylorF2) has been used in the search for binary neutron stars [12, 13, 15, 135], primordial black holes [14, 15, 135] and black holes [135] **primordial black holes and black holes sounds a bit funny**. The TaylorF2 waveform is parameterized by the binary's component masses m_1 and m_2 (or equivalently the total mass $M = m_1 + m_2$ and the symmetric mass ratio $\eta = m_1 m_2 / M^2$) and an upper frequency cutoff f_c. Amplitude evolution is modelled to leading order and phase evolution is modelled to a specified post-Newtonian order. In order to test the ability of TaylorF2 waveforms to detect numerical relativity signals,

we performed several analyses of the NINJA data with varying the parameters of a bank of TaylorF2-based templates. The results of these searches are summarized in Table 5, each column giving the results from a different search with a summary of the chosen parameters. We first describe the parameters that are varied and then present a more detailed discusion of the results.

All TaylorF2 NINJA analyses used restricted templates (i.e. the amplitude is calculated to leading order), however the phase was calculated to various different post-Newtonian orders [136]. Phases were computed to either two or three point five post-Newtonian order since these are, respectively, the order currently used in LSC-Virgo searches [15] and the highest order at which post-Newtonian corrections are known. After chosing a waveform family, one chooses a region of mass-parameter space to cover with the template bank. The NINJA analysts varied this choice, with one run using the range used by the LSC-Virgo "low-mass" search range of $m_1, m_2 \geq 1M_\odot, M \leq 35M_\odot$. Other searches extended the maximum total mass to around $100M_\odot$. Inspiral signals above this mass will have little, if any, power in the sensitive band of the NINJA data. Many searches also used a minimum mass of $M \geq 20M_\odot$, since there were no signals in the NINJA data with mass smaller than this.

The masses of the binary enter the leading order contribution to the phase evolution of TaylorF2 templates as $\mathcal{M} = (m_1 m_2)^{3/5}(M)^{-1/5}$, where $\mathcal{M}$ is called the chirp mass. Signals may be paramerized by $\mathcal{M}$ and η. The LSC-Virgo template bank generation code [126] restricts template generation to signals with $\eta \leq 0.25$. Above this value, it is not possible to invert $\mathcal{M}$ and η to obtain real-valued component masses, although generation of TaylorF2 signals with "unphysical" values of η is possible. In two separate studies [137, 138], the match between Goddard-NASA and Pretorius waveforms [137], and Caltech-Cornell waveforms [138], against TaylorF2 stationary-phase templates were analyzed. It was observed that across a wide range of masses, the match between numerical signals and TaylorF2 templates could be increased by relaxing the condition $\eta \leq 0.25$. One NINJA contribution uses such a template bank.

It is necessary to specify a cutoff frequency at which to terminate the TaylorF2 waveform. In the LSC-Virgo analyses, this is chosen to be the innermost stable circular orbit (ISCO) frequency for a test mass in a Schwarzschild spacetime

$$f_{ISCO} = \frac{c^3}{6\sqrt{6}\pi GM}. \tag{7}$$

This was thought to be the point at which the TaylorF2 waveforms diverged from the true evolution. More recently, comparisons with numerical relativity waveforms have shown that extending the waveforms up to higher frequencies improves the sensitivity of TaylorF2 templates to higher mass signals [137, 138]. Two specific choices have been made in the NINJA analysis. The effective ringdown (ERD) frequency was obtained by comparing post-Newtonian models to numerical waveforms [137]. Additionally, for the "unphysical" waveform templates, a weighted ringdown ending (WRD) frequency between ISCO and ERD was employed [138].

Each column in Table 5 gives the result of analyzing the NINJA data with the parameters above varied, with the key result being the number of detected signals. For simplicity, we define a detected signal as one for which there is a trigger observed within 50 ms of the coalescence time of the injection. For a single detector, this will lead to a small number of falsely identified injections, but for coincidence results the false alarm rate is so low that we can be confident that the triggers are associated to

Template	TaylorF2	TaylorF2	TaylorF2	TaylorF2	TaylorF2	TaylorF2	TaylorF2
Freq. Cutoff	ISCO	ISCO	ERD	ERD	ERD	WRD	WRD
PN Order	2 PN	2 PN	2 PN	3.5 PN	2 PN	3.5 PN	3.5 PN
Component Mass $M_\odot$	1-34	10-60	10-60	10-60	1-99	10-60	10-60
Total Mass $M_\odot$	2-35	20-90	20-90	20-90	1-100	20-90	20-90
η range	0 - 0.25	0 - 0.25	0 - 0.25	0 - 0.25	0 - 0.25	0 - 0.25	0 - 1
Found Single (H1, H2, L1, V1)	69, 66, 75, 69	72, 43, 66, -	83, 51, 81, -	91, 56, 87, -	95, 88, 105, 105	90, 55, 88, -	90, 56, 88, -
Found Coincidence (LIGO, LV)	49, 53	59, -	79, -	82, -	81, 91	82, -	84, -
Found Second Coinc (LIGO, LV)	48, 51	59, -	77, -	81, -	84, 97	81, -	81, -

Table 5. Results of inspiral search for NINJA waveforms. There were 126 injections performed into the data. The table above shows the number of injections which were recovered using various different waveform families, termination frequencies ISCO, ERD and WRD (as described in the text), and post-Newtonian orders.

the injection. We now describe these results in the order that they appear in Table 5.

The first search used second order post-Newtonian templates with a maximum mass of $35M_{\odot}$, terminated at ISCO. Despite the fact that only one NINJA injection had a mass within the range of this search, a significant number of signals were still recovered in coincidence both before and after signal consistency tests. Although the templates are not a particularly good match to the injected signals, they are still similar enough to produce triggers at the time of the injections. The second search extended the upper mass limit of the parameter space to $M \leq 90M_{\odot}$, but left all other parameters unchanged. The number of detected signals increases significantly as more signals now lie within the mass range searched.

The third search extended the ending frequency of the waveforms from ISCO to ERD and the number of signals detected increased from 59 to 77, as expected since these waveforms can detect some of the power contained in the late inspiral or early merger part of the signal [137, 138]. The fourth search extended the post-Newtonian order to 3.5 PN, slightly increasing the number of detected signals to 81. With the limited number of simulations performed in this first NINJA analysis, it is difficult to draw a strong conclusion, although there does seem to be evidence that the higher post-Newtonian order waveforms perform better. This is consistent with comparisons of post-Newtonian and numerical relativity waveforms [137–140].

The final analysis examines the effect of extending the template bank to unphysical values of the symmetric mass ratio. To examine the effects of extending the bank, two analyses were performed: one using $\eta \leq 0.25$ and one with $\eta \leq 1$. The same range of total mass M, weighted ringdown frequency cutoff and post-Newtonian order were used. Extending to unphysical values of η increases the number of templates in the bank by a factor of ~ 2; the original and modified template banks are shown in Figure 4. With the extended template bank the number of recovered injections increased slightly. More significantly, Figure 4 shows that the signal-to-noise ratio of the signals recovered with the extended bank is greater than or equal to that with the standard bank. In some cases, there is a significant increase, with a gain in SNR of over 10%.

Finally, we note that very few of the signals were removed by the χ^2 signal based veto with the thresholds used in the LSC-Virgo pipeline. The last two lines of Table 5 show the number of recovered signals before and after these signal consistency tests are performed. The post-Newtonian templates and numerical relativity signals are similar enough that virtually all of the injected signals survive the signal based vetoes.

To illustrate the results of these analyses in more detail, Figure 5 shows which signals were detected and which were missed by the 3.5 PN TaylorF2 ERD NINJA analysis, as a function of injected total mass and effective distance, a measure of the amplitude of the signal in the detector [129]. Only one signal lying in the sensitive region of the search was not recovered. This missed signal was one of the Princeton waveforms (labelled PU-e0.5 in Figure 1) for which the maximum amplitude occurs at the start of the waveform rather than at coalescence. The injection finding algorithm compares this time to the trigger time and, even though triggers are found at the time of the simulation, there are no triggers within the 50 ms window that was used. The missed injection with a chirp mass of around $115M_{\odot}$ and an effective distance of 200 Mpc is the signal which is rejected by the signal based vetoes in this analysis. It is one of the UIUC_puncture waveforms. Since the mass lies well outside the range of the search it is not unexpected that this signal does not survive the analysis.

When matched filtering for the inspiral part of a binary coalescence, the two

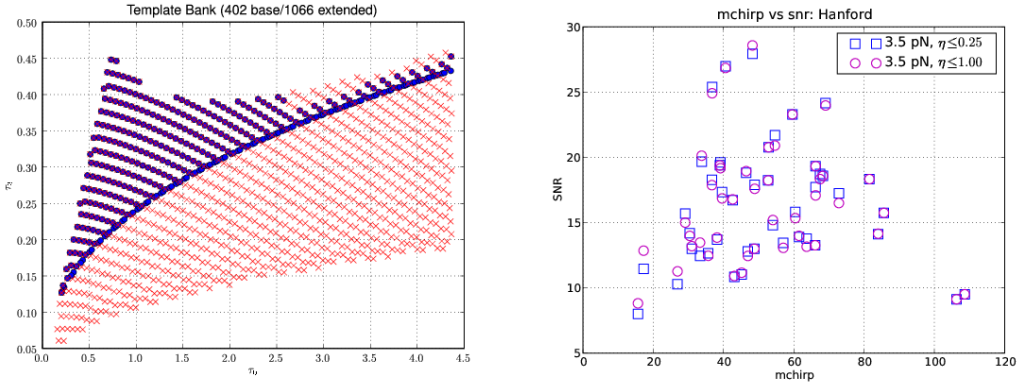

Figure 4. Left: The template bank generated by the LSC search pipeline and the bank obtained by extending to $\eta \leq 1.00$. In this figure the bank is parametrized by τ_0 and τ_3 which are related to the binary masses by $\tau_0 = 5M/(256\eta v_0^8)$ and $\tau_3 = \pi M/(8\eta v_0^5)$, where $v_0 = (\pi M f_0)^{1/3}$ is a fiducial velocity parameter corresponding to a fiducial frequency f_0, usually chosen to be the lower frequency cutoff of the detector sensitivity. **Right:** The signal-to-noise (SNR) ratio at which NINJA injections were recovered using the $\eta \leq 0.25$ bank (squares) and the $\eta \leq 1$ extended bank (circles) in the Hanford detectors, given by $\rho = (\rho_{\rm H1}^2 + \rho_{\rm H2}^2)^{1/2}$. The SNR of the signal recovered using the extended bank is at least as large as the standard bank, with significant ($> 10\%$) increases for certain injections.

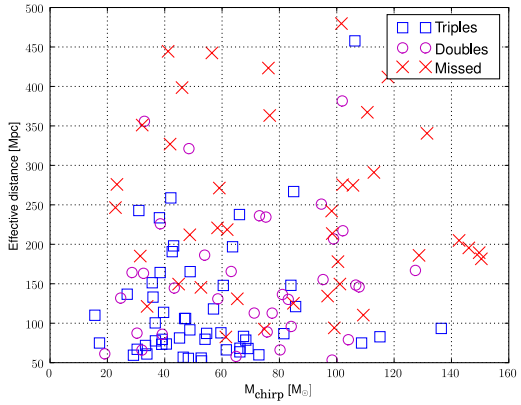

Figure 5. Figures showing the found and missed injections as a function of the injected effective distance in Hanford and the chirp mass. For the lower masses, we see that the majority of the closer injections are found in coincidence in all three of the detectors. There is then a band of injections which are found only in two decectors – H1 and L1 and not the less sensitive H2 detector. For higher masses, the results are less meaningful as the template bank was only taken to a total mass of $90M_\odot$, which corresponds to a maximum chirp mass of $40M_\odot$.

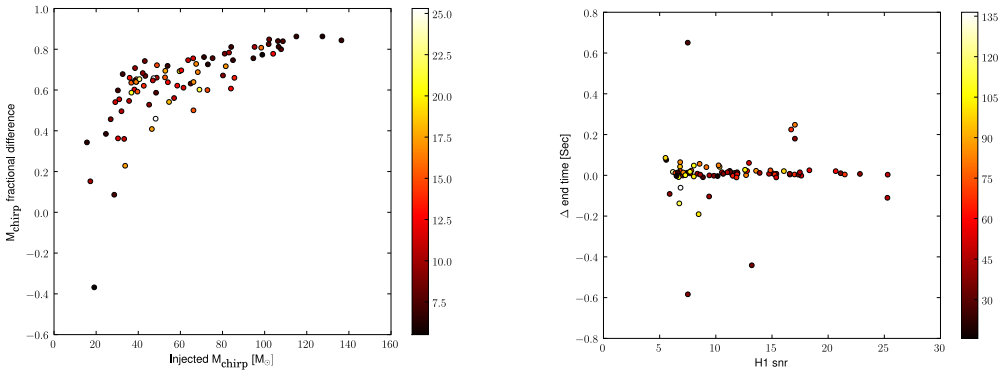

Figure 6. Figures showing the accuracy with which the chirp mass and end time of the numerical relativity injections were recovered using the effective one body waveforms. In both plots, the color scale is given by the total mass of the system. The end time is relatively well recovered for the lower mass systems, while as the mass increases, the timing error can become as large as 50ms. The chirp mass is recovered accurately only for a couple of injections. The vast majority have an error of 40% or greater.

parameters recovered most accurately are the chirp mass and the coalescence time. In Figure 6 we show the accuracy with which these quantities are recovered when using the 3.5 PN Taylor F2 templates. For lower mass signals, the end time is recovered reasonably accurately, with accuracy decreasing for the high mass systems. The chirp mass recovery is poor for the majority of signals, with good parameter estimation for only a few of the lowest mass simulations.

4.1.2. Neyman-Pearson Interpretation of Inspiral Searches In the previous section, we have described a significant number of searches performed using TaylorF2 templates. These searches achieved relatively similar results in terms of our simple found and missed criteria. Here, we discuss a more sophisticated method of determining efficiency of our algorithms to recover a realistic signal. For the purposes of this section, we restrict to two of the TaylorF2 searches described in Table 5.

The first search, summarized in the first column of Table 5, was chosen to mimic the standard low mass CBC search [135]. Below we will refer to it as the low mass search. The second search considered here is summarized by the fifth column of Table 5. It uses 2 PN TaylorF2 templates covering the widest mass range allowed by the instrumental noise curves. Thus it can be thought of as the simplest extension of the standard low mass CBC search. These searches have both used data from all four interferometers allowing us to make a fair comparison of their results.

To evaluate the detection efficiency of the searches we adopted the Neyman-Pearson detection criteria [123] which has been shown to be the optimal detection strategy under quite general assumptions. According to this criteria, an injected signal is marked as found if the statistic, Λ, for its corresponding trigger exceeds some set threshold, Λ^*. This threshold is usually determined by the value at which the false alarm probability — the probability that a noise event will be mistaken for a real signal — is considered to be tolerable. Here we set the threshold to be the highest value of the statistic found in the data that contain only noise. We identified this

background data by discarding all triggers within 5s of the coalescence time of the injections. Thus we mark an injection as found only if it resulted in a trigger with statistic higher then any background trigger found in the data. We expect that even this crude method of background estimation should provide us with consistent criteria for elimination of spurious detections.

Optimality and efficiency of this method depends crucially on how close the statistic, Λ is to the optimal one. It is well known that SNR is the optimal statistic for detection of signals in a single interferometer in the presence of colored gaussian noise. Its simplest generalization to the case of coincident triggers from multiple interferometers is combined SNR. In the presence of non-Gaussian noise, the effective SNR statistic has been found useful [15, 124].

We applied the Neyman-Pearson criteria to triggers found in our searches both before and after the calculation of signal based vetoes. The resulting numbers of found numerical relativity injections are listed in Table 6. For triggers generated in the first stage we used combined SNR ratio as the detection statistic. For triggers generated after the second stage we used both effective SNR and combined SNR statistics.

	Low Mass		High Mass	
Stage, statistic	Statistic Threshold, Λ^*	Found Injections	Statistic Threshold, Λ^*	Found Injections
FIRST, ρ_c	9.18	73	9.8	91
SECOND, ρ_c	9.18	69	9.8	93
SECOND, ρ_{eff}	10.05	27	10.05	85

Table 6. Number of found injected signals after first and second stages of the pipeline using Neyman-Pearson criteria

It is interesting to compare the results of Table 6 to those presented in Table 5. Note that the number of injections "found" at the end of the low mass search using Neyman-Pearson criteria instead of 50 ms time window around injection has increased from 51 to 69. Since low mass templates are a poor match to the injected signals, the coalescence time will be poorly estimated. This will result in triggers outside the 50 ms window, which are nevertheless are loud enough to lie above the background.

Signal-based vetoes are applied at the second stage of the inspiral pipeline. By comparing the outputs of the first and the second stages of the pipeline we can evaluate the effects of the signal-based vetoes on the overall sensitivity of the searches. Note that in both searches the threshold combined SNR did not change at the second stage. The additional vetoes applied at this stage have reduced the total number of background triggers but not the significance of the loudest background trigger. Since these vetoes were designed to eliminate loud non-gaussian artefacts, their limited effect here is not unexpected. For the low mass search, we find a slight decrease in the number of injections found after the second stage of the analysis, probably due to the fact that the templates are not a good match for the signals. Much more intriguing is a slight positive effect of the same signal based vetoes on triggers associated with injections in the high mass search. At the same threshold we recover 93 injections at the second stage compared to 91 at the first. Additional investigations revealed that, despite having fewer triggers in each detector at the second stage, the total number of coincident triggers actually increases. Essentially, signal based vetoes push triggers due to injections closer in time on average and this results in better detection efficiency. We do not observe this in the case of the low mass search.

Finally, we would like to comment on the use of effective SNR as detection

statistic. As can be seen from the numbers in the last row of Table 6 using this statistic significantly reduces the overall efficiency of both searches. Since this statistic has been designed for highly non-gaussian noise, its applicability and utility in the present case is questionable.

4.1.3. Inspiral-Merger-Ringdown Templates The calculation of the full binary coalescence waveform requires numerical methods. At the present time, the numerical simulation of binary waveforms are, however, rather expensive and it is currently not feasible to model a coalescing binary over hundreds of orbits with sufficient accuracy. It is also unnecessary as PN theory already gives a valid description of the system when the black holes are sufficiently separated. During their final orbits before merger the black holes' velocities increase and the PN expansion becomes less reliable. At this stage the non-perturbative information contained in numerical simulations is required. A successful approach has been to combine the analytical and numerical results to obtain full waveform templates. Two different families of waveforms have been used in analyzing the NINJA data: the effective one body (EOB) [141, 142] and phenomenological [143, 144] models.

By combining together rather accurate results from PN theory and perturbation theory, the EOB model [141, 142] predicted, nearly a decade ago, inspiral, merger and ringdown waveforms. More recently, the non-spinning EOB model has been further improved by calibrating it to NR results, achieving rather high matching perfomances without maximizing on binary parameters, but only on initial phase and time of arrival [69, 110, 137, 139, 145–147]. The original implementation of the EOB model in the LIGO Algorithms Library (LAL) [121] gave the waveform for a binary evolved only up to the light ring frequency. More recently an implementation of the full EOB waveform [145] called EOBNR has been added. Extensive tests have confirmed that the EOBNR implementation in LAL accurately reproduces the EOB model which was used in Ref. [145] to match the NR waveforms produced by the NASA/Goddard group of black holes with mass ratios $m_1 : m_2 = 1 : 1,\ 2 : 3,\ 1 : 2,\ 1 : 4$.‡ The LAL implementations of both EOB and EOBNR were used to search for black hole binary signals in NINJA data.

Another approach for constructing the full waveform is to stitch together the results of PN and NR calculations. The model presented in [143, 144] consists of matching the PN and NR waveforms in an appropriate matching regime (where both PN and NR are sufficiently accurate) to obtain a "hybrid" waveform, and then fitting this hybrid waveform by a phenomenological model in the frequency domain determined entirely by the physical parameters of the system. This procedure has been carried out for non-spinning black holes, and a two-dimensional template family of waveforms that attempts to model the inspiral, merger and ringdown stages for non-spinning binary black holes has been obtained. Each waveform is parametrized by the physical parameters of the system, i.e. the masses m_1 and m_2 of the black holes.

Since the EOBNR and phenomenological models provide complete waveforms, the search was performed to higher masses ($200M_\odot$ and $160M_\odot$ respectively) than for inspiral only searches. In principle, the search could be extended to even higher masses, but issues with the current waveform generation procedures prevent this.

‡ Note that although the higher order harmonics were included in the EOB model used in Ref. [145], they have not yet been implemented in the search.

Template	EOB	EOBNR	Phenom
Freq. Cutoff	Light ring	Full waveform	Full waveform
Filter Start Freq.	40 Hz	30 Hz	30 Hz
Component Mass $M_\odot$	10-60	15-160	20-80
Total Mass $M_\odot$	20-90	30-200	40-160
Minimal Match	0.97	0.99	0.99
Found Single (H1, H2, L1, V1)	91, 64, 82, -	97, 68, 92, 102	92, 61, 87, -
Found Coincidence (LIGO, LV)	83, -	88, 106	81, -
Found Second Coinc (LIGO, LV)	80, -	85, 102	80, -

Table 7. Results of the search for NINJA signals using IMR template banks. There were 126 injections performed into the analyzed data. The signal-based vetoes have little influence in the rejection of triggers, confirming their efficiency in separating inspiral-like signals from other kind of glitches.

In the future, these issues will be addressed to allow the generation of higher mass templates. The minimum component mass was also increaed, in an effort to reduce the size of the template bank by limiting the number of highly asymmetric signals. Finally, the template bank for all these searches was constructed using the standard second order post-Newtonian metric, and hexagonal placement algorithm [127]. At high masses, the parameter space metric for the full waveforms will differ significantly from the standard 2 PN metric. However, the current template bank placement suffices for detection purposes, although probably not for good parameter estimation.

The key parameters and results of analyzing the NINJA data with the EOB, EOBNR and phenomenological waveforms are also given in Table 7. For the EOB model truncated at light ring, the other parameters were chosen to match the TaylorF2 analyses described in Section 4.1.1. Therefore, it is unsurprising that the results are very similar to the TaylorF2 search extended to ERD (the fourth column of Table 5). The EOBNR results show some improvement for detecting the numerical relativity signals over the usual post-Newtonian or EOB waveforms. For the phenomenological waveforms, time windows of 120ms in single detector and 80ms in coincidence have been used to associate triggers to injections. These parameters differ from those employed in other searches to compensate for a relatively large observed error in the estimation of the coalescence time. By comparing the results with the standard PN analyses presented in Section 4.1.1, we conclude that in the present case the phenomenological waveforms [143, 144] do not seem to provide a clear benefit over the usual post-Newtonian waveforms extended to higher cutoff frequency and/or to unphysical regions of the parameter space [137, 138]. In all cases, the signal-based vetoes have little influence in the rejection of triggers, confirming their efficiency in separating inspiral-like signals from other kind of glitches.

Plots of found and missed injections for the searches are shown in Figure 7. For the most part, simulated signals in the mass range covered by the template banks are well recovered. Some of the missed signals at lower distance correspond to waveforms from simulations of spinning black holes. Since all searches make use of non-spinning waveforms this drop is expected. Finally, we turn to parameter estimation. Figures 8 and 9 show the parameter recovery accuracies for the EOBNR and phenomenological searches respectively. In both cases, the accuracy of recovering the chirp mass of the simulations is greatly improved over TaylorF2 waveforms shown in Figure 6. This is likely related to the increased mass range of the searches, as well as the use of full waveforms. The timing accuracy for EOBNR is comparable with the TaylorF2 results,

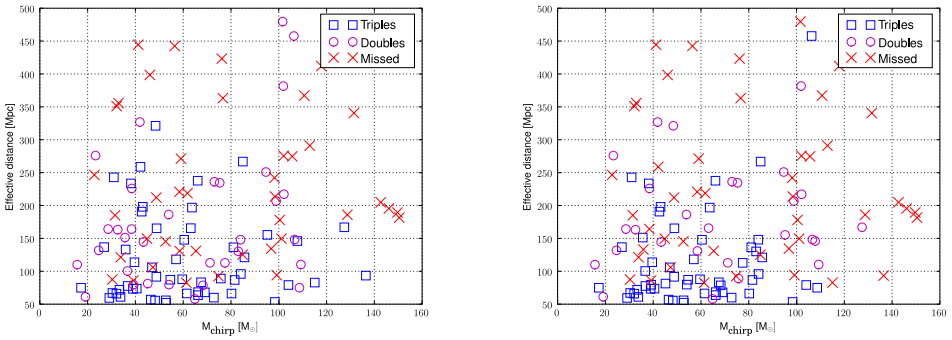

(a) Search with EOBNR templates.

(b) Search with phenomenological templates.

Figure 7. The figure shows found and missed injections as a function of the injected eective distance in Hanford and the chirp mass for (a) the EOBNR search, and (b) the search with phenomenological waveforms.

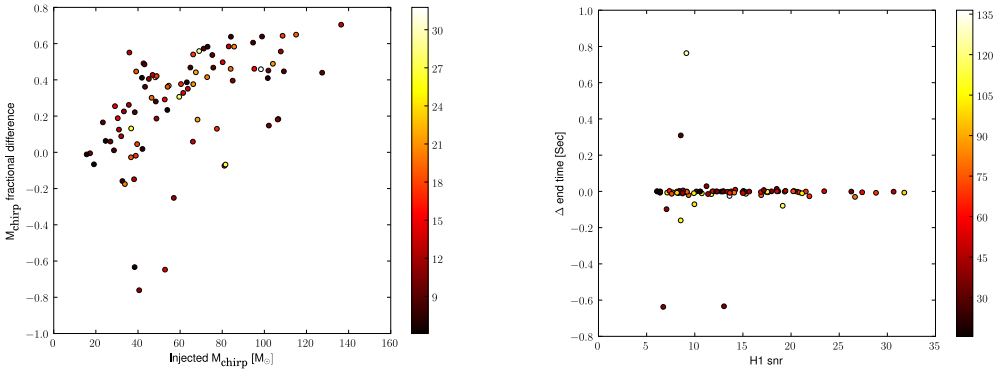

Figure 8. Figures showing the accuracy with which the chirp mass (left panel) and end time (right panel) of the numerical relativity injections were recovered using the EOBNR templates. In both plots, the colour scale is given by the total mass of the system. Most of the injections with total mass less than 200 $M_\odot$ were recovered with a chirp mass accurate within a few tens of percent. Higher mass injections are necessarily recovered with underestimated chirp mass, because the template bank did not cover the entire simulation region. The end time for injections with total mass less than 200 $M_\odot$ was typically recovered to within a few milliseconds. The end time for injections with total mass above 200 $M_\odot$ (outside the range of the template bank) was typically recovered to within 10 or 20 milliseconds.

while for the phenomenological waveforms, the known timing bias affects the results.

Both the EOBNR and phenomenological models will be improved in the future. Further accurate EOBNR models have already appeared in the literature [110, 139, 145–147] since the time the EOBNR model used in this analysis was implemented, and extensions to include spin and eccentricity are under development. There are a number of obvious improvements in the phenomenological waveforms that can be made. The first issue is to calculate the parameter space metric for the phenomenological

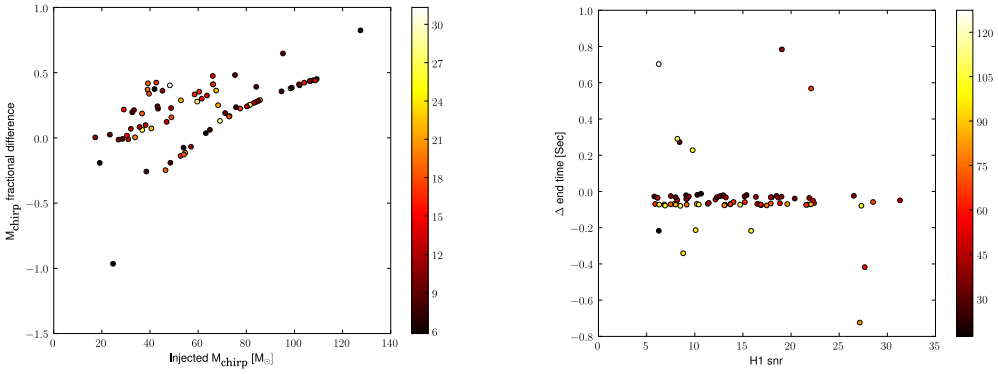

Figure 9. Figures showing the accuracy with which the chirp mass (left panel) and end time (right panel) of the numerical relativity injections were recovered using the phenomenological templates. In both plots, the colour scale is given by the total mass of the system. The chirp mass is typically recovered within 20%, for signals within the template space. The timing plot shows the systematic offset discussed in the text.

waveforms. This would enable use of an optimal template bank and allow for improved coincidence and parameter estimation algorithms. The construction of the phenomenological waveform model can itself be significantly improved by extending the fitting to higher mass ratios and spins, quantifying the error bars on the phenomenological parameters, matching to post-Newtonian theory as early as possible and including higher modes in the waveform. The results of the NINJA analysis also show a glaring need to improve accuracy in estimating the end time of the signal, although this is not straightforward since there is no clear definition of the time of merger for the phenomenological waveforms. Work on the improvements to both the EOBNR and phenomenological searches is in progress, and will be applied in and guided by future NINJA projects.

4.1.4. Ringdown Templates As described in section 4.1, the ringdown templates are exponentially damped sinusoids parametrized by the ringdown frequency f and quality factor Q. Two groups used the standard LSC ringdown search pipeline [131] to filter the NINJA data against a bank of ringdown templates with frequency between 50 Hz and 2 kHz, and quality factor between 2 and 20. For a maximum mismatch of 3% this yielded 583 templates. The analysis was performed in overlapping blocks of 2176 seconds; the frequency cutoff was 45 Hz for the LIGO noise curves and 35 Hz for the Virgo noise curve.

The goals of these analyses were to ascertain the detectability of the injected numerical waveforms using ringdown templates at single and coincident detector levels, and the accuracy with which the final black hole parameters can be estimated. We also compare the parameters recovered from the ringdown search to those from searches for the other phases of the binary coalescence, the inspiral and merger. This comparison is made in section 4.3.

An injection is defined as found if a set of coincident triggers lies within 10 ms of the peak time of the injection (which was supplied to us by the NR groups). If more than one set of coincident triggers satisfies this criterion, that with the largest

value of $\sum_i \rho_i^2$ is selected, where ρ_i is the signal to noise ratio in the i^{th} detector. Of the 126 injections made into the three LIGO detectors, 45 were found in triple coincidence, 24 in H1 and L1 (only), and 7 in H1 and H2 (only). Figure 10(a) shows the missed and found injections in a plot of the injected Hanford effective distance d_{eff} versus the predicted ringdown frequency§, and figure 10(b) shows the Livingston effective distance of the injections versus total initial mass. As expected, we see that in general, the closest injections were found in triple coincidence, those with a large Livingston effective distance were found in H1 and H2 only, while those with a large Hanford effective distance were not found in H2, and the furthest injections were missed in at least two detectors. The plots show that there are three missed injections which, given their frequencies and effective distances, we would have expected to find. However, all three of these are (non-spinning) injections with mass ratio of 4:1, and thus the energy emitted in the ringdown is less than would be emitted by a binary of the same total mass but with a mass ratio of 1, which is not taken into account in the calculation of effective distance.

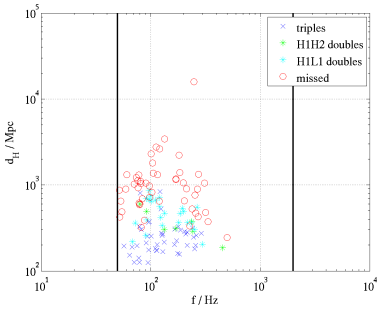

(a) Hanford effective distance versus (predicted) ringdown frequency.

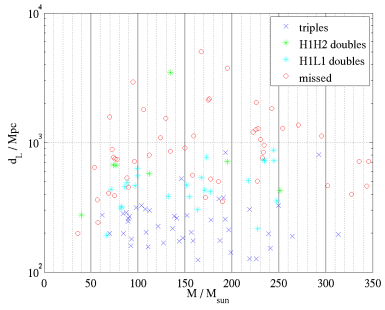

(b) Livingston effective distance versus mass.

Figure 10. Injections found in triple coincidence (blue crosses), in double coincidence in H1H2 (green stars), in double coincidence in H1L1 (cyan stars), and missed (red circles).

Assuming that the dominant ringdown mode is the fundamental mode, $l = m = 2$, the frequency and quality factor of the waveform can be expressed in terms of the mass M and dimensionless spin factor a of the black hole using Echeverria's analytic fit [149] to Leaver's numerical calculations [150],

$$f = \frac{1}{2\pi}\frac{c^3}{GM}\left[1 - 0.63\,(1-a)^{\frac{3}{10}}\right] \tag{8}$$

$$Q = 2\,(1-a)^{-\frac{9}{20}}\,. \tag{9}$$

We can invert these equations and calculate the M and a from the template parameters of a given trigger. In figure 11(a) we plot the mass detected in H1 versus the total initial mass for all found injections. The plot shows that despite the presence of the inspiral and merger, the parameter accuracy attained using ringdown templates was quite good for the mass space covered. In figure 11(b) we plot the difference between the time of waveform peak amplitude and the start time of the ringdown as found by

§ the ringdown frequency was not supplied to us from the numerical groups, however we can estimate it from the initial masses and spins as described in [148].

the template. The three data points with a large time difference and masses lying in the range 80 and 110 $M_\odot$ are part of the PU_T52W non-spinning equal mass group (with id's 114 120 and 125) where the peak amplitude occurred early in the waveform (*i.e.* prior to the merger), and the point at a mass of 264 $M_\odot$ is one of the UIUC moving puncture injections.

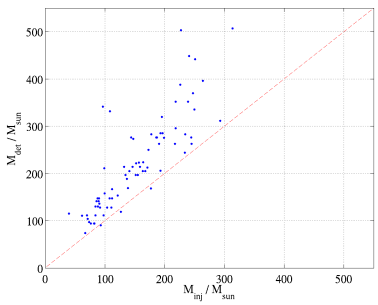

(a) Detected ringdown mass versus total injected mass.

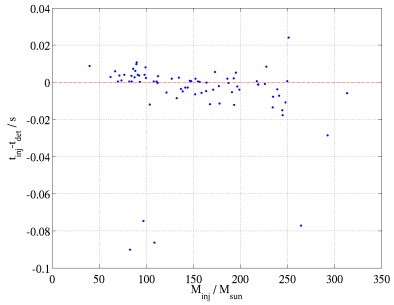

(b) Difference between the peak time of the injection and the detected ringdown trigger time versus total injected mass.

Figure 11. Ringdown parameter accuracy.

4.2. Search pipelines using unmodeled waveforms

Burst searches are designed to detect gravitational wave transient signatures with minimal assumptions on their origin and waveform. They do not use templates and instead target excesses of power in the time-frequency plane. The LSC and Virgo collaborations have developed several algorithms for burst searches, which use different transformations for the generation of time-frequency data maps. The identification of coherent signatures across multiple detectors has proven to be very effective at suppressing false alarms.

Since they do not assume a template, and they target short transients, burst searches are suited for the detection of the merger phase of the coalescence, and have the potential to probe a large parameter space, inclusive of spin and ellipticity, at no additional computational cost. For this reason, the NINJA data was analyzed by two burst algorithms: Q-pipeline and HHT.

The Q-pipeline [151, 152] is one of the algorithms used in the burst search for the LIGO fifth science run [add ref burst S5 year 1 paper in preparation]. It is a multi-resolution time-frequency search for statistically significant excess signal energy, equivalent to a templated matched filter search for sinusoidal Gaussians in whitened data. The template bank is constructed to cover a finite region in central time, central frequency, and quality factor such that mismatch between any sinusoidal Gaussian in this signal space and the nearest basis function does not exceed a maximum mismatch of 20% in energy. For the purpose of the NINJA analysis, and to explore detectability and parameter estimation, the Q-pipeline analysis was focused on the detection efficiency at the single detector, for all four detectors, using a nominal SNR threshold comparable to the one used in the matched filter searches.

The Hilbert-Huang Transform (HHT) [153, 154] is an adaptive algorithm that decomposes the data into Intrinsic Mode Functions (IMF's), each representing a

unique locally monochromatic frequency scale of the data. The original data is recovered with a sum over all IMF's. The Hilbert transform as applied to each IMF unveils instantaneous frequencies (IF) and amplitudes (IA) as a function of time, thus providing high time-frequency resolution to detected signals without the usual time-frequency-uncertainty as found in basis set methods like the Fourier transform. Since the HHT pipeline [155] is a new development, currently being tested, its application to NINJA data was focused solely on the analysis of H1 and L1 data.

In this section we briefly describe how the algorithms were applied and highlight their performance, while in section 4.3 the performance of burst searches is compared to that of matched filtering algorithms that target inspiral and ringdown or full waveform.

4.2.1. Q-pipeline The Q-pipeline processed data from the LIGO and Virgo detectors with the same configuration file as in the S5 analysis, with 64 s analysis blocks, frequency range 48–2048 Hz and Q range 3.3–100. The resulting triggers, once clustered, indicate a time-frequency interval and a significance of the excess power in that time-frequency tile, which can be easily converted into a signal-to-noise ratio, equivalent to ρ_{match} for matched filter with sine-gaussians.

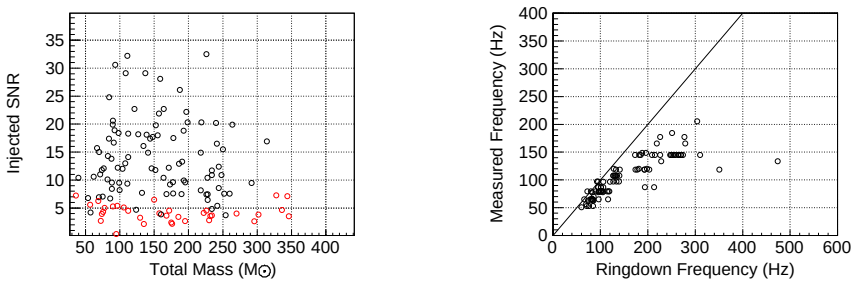

Figure 12. Left: Missed and found injections by Qpipeline at H1. Right: Qpipeline measured frequency vs the nominal ringdown frequency F_{RD}.

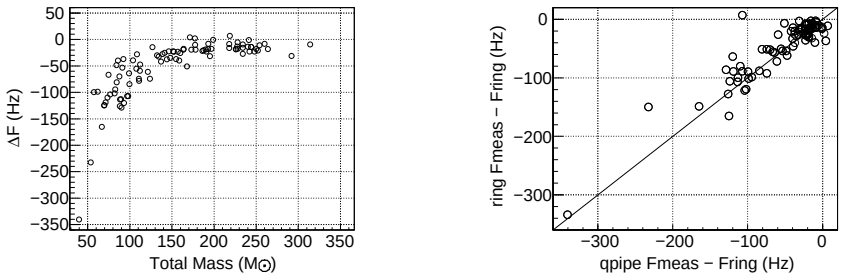

Figure 13. Left: difference between Qpipeline measured frequency and F_{RD}, plotted vs total injected mass. Right: scatter plot of the same difference for the ringdown code and for the burst code.

Figure 12-a shows missed and found injections in the H1 detector function of Total mass and the SNR of the injected waveforms, if the detection threshold is set at

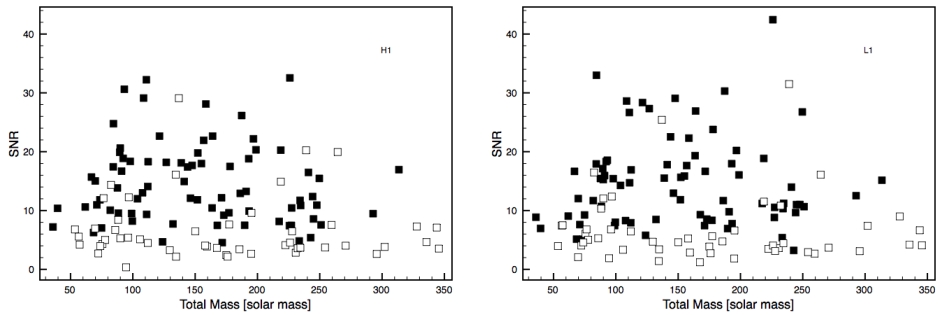

Figure 14. Missed-found plots for H1 and L1 using the Hilbert–Huang transform.

SNR=5.5. Figure 12-b is a scatter plot of the central frequency of the most significant tile reported by Qpipeline versus the ringdown frequency explain how the FRD is calculated. Figure 13-a shows the difference between measured frequency and FRD vs mass and Figure 13-b is a scatter plot of this difference for Qpipeline and the ringdown code. The conclusion we can draw from these plots is that both Qpipeline and the ringdown code are most sensitive to the portion of the signal that is in the most sensitive region of the detector (50-200Hz): the ringdown for higher masses, or the inspiral for lower masses.

4.2.2. Hilbert-Huang Transform We applied an automatic two-stage HHT pipeline to pre-whitened, 1000 Hz lowpass zero-phase FIR filtered NINJA data to detect and characterize the signal. In the first detection stage, the IA's from each detector in turn are divided into blocks with similar statistical properties according to the Bayesian Block algorithm [156]. These blocks are then scanned for excess power, with triggered blocks yielding start and end times, thus coincidences between detectors, the maximum frequency, and the signal-to-noise ratio (SNR) of the signal. The second characterization stage zooms into the signal region of interest in each detector and derives the IF, highly detailed time-frequency-power (tfp) maps and time-frequency-power cluster-enhanced maps (wKDE). The overlap of the individual wKDE's is finally used to estimate the time lag between the signals in the detectors and to construct a coherent addition of the two detector data streams used in a final characterization of the signal.

We used the sharpness in time and frequency to reject false events due to overly short triggers, failed coincidences or mismatched time-frequency ranges to gain sensitivity. We identified the latter as a possible powerful veto tool for future pipeline runs on gravitational wave data if fully exploited. We were ultimately able to identify 80 events in coincidence, with 3 of these to be ruled false positives by hindsight (see Figure 14). Out of the missed 50 events, 39 are SNR$<$ 10, 5 are SNR$<$ 10 in one detector and SNR$>$ 10 in the other, 6 were SNR$>$ 10. We therefore reason that most of the of missed events are low SNR cases in which no blocks were triggered. Most of the wKDE maps show the evolution of the frequency in time in high precision (see Fig. 15 for one particular example). Time lag estimates and coherent additions show strong potential and can be seen as proof of principle, but need further refinement to work reliably in an automatic pipeline. SNR estimates are difficult since only the

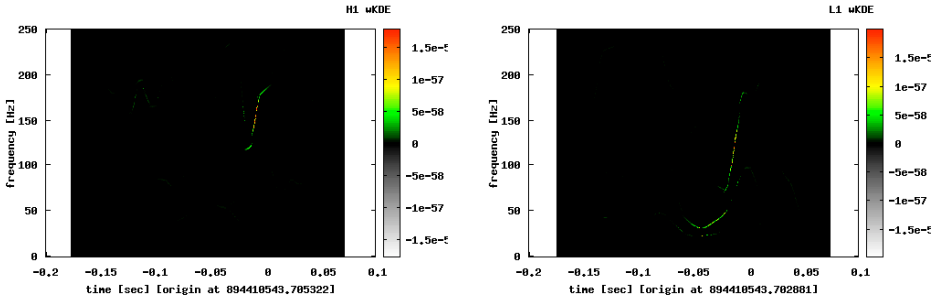

Figure 15. The wKDE maps of event 894410543 are shown with H1 in the left panel and L1 in the right panel. We clearly see the burst part of the signal, thus the actual merger. Ringdown and inspiral may be obscurred by noise at low SNR. A black figure background is difficult to read; could use white instead.

burst region or diverse fragments of the signal are visible in our analysis. We refer to [157] for further details of this analysis.

4.3. Comparison Inspiral-Burst-Ringdown Results

need an intro here, and polish text. Also, need to describe figures 16 and 17

Table 8 shows the counts of found injections in single interferometers and in multi-interferometer networks, using triggers from Q-pipeline (burst), lalapps_ring (ringdown) and the matched filter inspiral and EOBNR. For all algorithms the same nominal threshold of $\mathrm{SNR}_{measured} \geq 5.5$ was imposed. In addition, the number of detected injections in AND (injections detected simultaneously from multiple algorithms) and OR (injections detected by at least one algorithm) in an inspiral-merger-ringdown analysis is reported. The statistics of this sample is too small to make inferences on which pipeline performs better in which parameter region; a more systematic study is needed. Also, this table does not take into account the effect of background noise transients and accidental coincidences, which are very different in real data and in gaussian noise, so this comparison is not complete. Nevertheless we have an indication that all pipelines have comparable chances to find these injections. The difference can come from parameter accuracy.

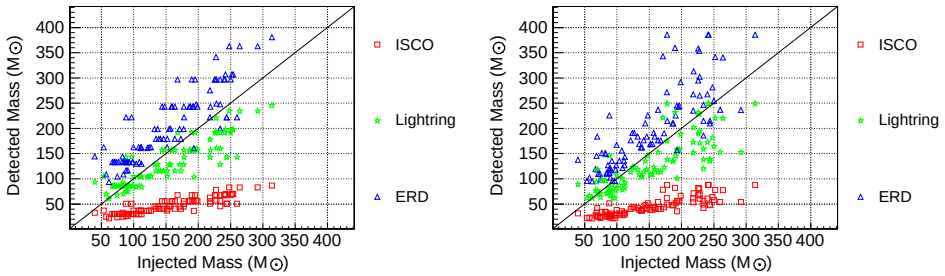

Figure 16. Mass vs mass: a) Qpipeline b) lalapps_ring.

Table 8. Number of injections found with $\mathrm{SNR}_{measured} \geq 5.5$. This table takes into account for each detector only signals with $\mathrm{SNR}_{injected} \geq 5.5$. If the same injection is found in more than one detector or algorithm, it is counted as coincidence. The inspiral triggers are from the 2 PN to ISCO (mass range?) and from the EOBNR matched filter to full IMR waveforms. emphasize threshold may be different for different algorithms, depend on false alarm rate and morphology of noise transient.

	H1	H2	L1	V1	H1L1	H1H2L1	H1L1V1	H1H2L1V1
$\mathrm{SNR}_{injected} \geq 5.5$	94	60	93	105	84	58	68	48
M Qpipe	88	55	85	92	77	51	57	40
R lalapps_ring	88	56	83	93	76	52	56	40
M-R AND	87	55	82	91	76	51	56	40
M-R OR	89	56	86	94	77	52	57	40
Inspiral (p20i)	85	43	82	–	75	43	–	–
I-M-R AND (p20i)	82	42	77	–	72	41	–	–
I-M-R OR (p20i)	91	57	88	–	80	55	–	–
EOBNR	90	56	88	100	79	54	64	45
I-M-R AND	86	53	81	88	75	49	56	39
I-M-R OR	92	58	91	104	81	56	65	47

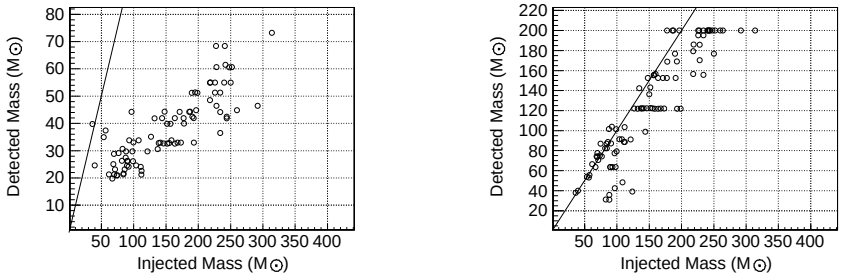

Figure 17. Detected vs injected mass at H1: a) inspiral b) EOBNR.

Figures 16 and 17 compare the mass detected by various algorithms to the injected total mass. Burst algorithms report a frequency, not a mass. But we can calculate the corresponding mass under the assumption the algorithm is detecting a given portion of the waveform, using double check and add references:

$$f_{ISCO} = \frac{1}{6^{3/2}\pi M_{\odot}} \tag{10}$$

$$f_{LR} = \frac{1}{3^{3/2}\pi M_{\odot}} \tag{11}$$

$$f_{ERD} = \frac{0.5967}{2\pi M_{\odot}} \tag{12}$$

We already mentioned both burst and ringdown code preferentially detect the portion of the signal that is in the detectors' most sensitive band. Figure 16 shows that for both algorithms, at the lowest injected masses this correspond to f_{ISCO}, but as the injected mass increases, the algorithms trigger between lightring and ringdown, as

expected. This comparison is more straightforward for matched filtering codes that use a template with a given mass, as in figure 17, where we show the matched filtering to inspiral templates (2 PN extracted at ISCO), in a search with mass range 20-80 $M_\odot$ and EOBNR in a search up to 200 $M_\odot$.

4.4. Bayesian pipelines

Bayesian inference is a powerful means of extracting maximum information from observational data, based on the calculation of posterior probabilities and probability density functions. Although these calculations are too computationally expensive to perform on all the data available, they are useful in the closer study of candidates identified by search pipelines based *e.g.* on a pre-determined template bank, like those described above.

In this case, two different approaches were taken to make two particular inferences on the NINJA data. These inferences are (i) the estimation of the parameters of the signal assumed to be present in the data, and (ii) the calculation of confidence in the presence of the signal, quantified by the *odds ratio* between the signal and noise models of the data.

Both approaches require the calculation of the posterior probability density function (PDF) on the parameter space of the signal, given the data d, which is

$$\begin{aligned} p(\vec{\theta}|d) &= \frac{p(\vec{\theta})p(d|\vec{\theta})}{p(d)} \\ &\propto p(\vec{\theta}) \exp\left(-2 \int_0^\infty \frac{\left|\tilde{d}(f) - \tilde{h}(f;\vec{\theta})\right|^2}{S_{\rm n}(f)}\, df \right) \end{aligned} \tag{13}$$

in the presence of Gaussian noise $S_{\rm n}(f)$, where $h(\vec{\theta})$ is the model used to describe the signal.

A Markov-Chain Monte Carlo approach to coherently analyze data from multiple detectors was used to evaluate the posterior PDFs. This technique relies on computing the likelihood $p(d|\vec{\theta})$ for the observed data d given a choice of model parameters $\vec{\theta}$ in order to find the posterior PDFs on the unknown signal parameters. In this way, set of parameters that yield the best fit to the data, and determines the accuracy of the parameter estimation.

Bayesian model selection, based on a different Monte-Carlo technique known as nested sampling [158], was used as a tool to measure the confidence of a detection using different waveform families. This approach requires the calculation of the *marginal likelihood* of the signal and noise models, obtained by computing the integral of the posterior PDF $\int p(\vec{\theta})p(d|\vec{\theta})d\vec{\theta}$ to find the total probability of the model. It was possible to calculate this integral for the nine-parameter model of a non-spinning binary coalescence signal described coherently in multiple interferometers. The ratio of likelihoods of the signal and noise models is known as the "Bayes factor," and is used to multiply prior odds, giving the posterior odds ratio between the two models, taking into account the observational data; in turn, high values of this Bayes factor correspond to different level of confidence in the detection. As a straightforward by-product of the nested sampling algorithm, it is also possible to infer the maximum likelihood values of the parameters of the detected signals, which was used to obtained

further information on the ability of different waveform approximants to recover the source parameters.

4.4.1. Parameter Estimation Using Markov Chain Monte Carlo The Northwestern group analyzed the injected numerical signals with a Markov-Chain Monte Carlo (MCMC) code [159, 160]. We used restricted inspiral waveforms at 1.5 post-Newtonian order for this search. The search was successful on NINJA injections with relatively low total mass in which the inspiral contained a significant fraction of the total signal-to-noise ratio. For high-mass injections, the search attempted to match the merger and ringdown portions of the injected waveform to inspiral templates, resulting in poor parameter estimation.

Our templates are based on restricted post-Newtonian (PN) waveforms at the 1.5 PN order in phase and 0 PN order in amplitude. These waveforms currently include only the spin of the larger body, allowing us to use the analytical simple-precession waveform [161]. The parameter space thus consists of twelve independent parameters:

$$\vec{\theta} = \{\mathcal{M}, \eta, \mathrm{R.A.}, \sin \mathrm{Dec}, \sin\theta_{J_0}, \phi_{J_0}, \log d_L, a_{\mathrm{spin}}, \cos\theta_{\mathrm{SL}}, \phi_c, \alpha_c, t_c\}, \quad (14)$$

where $\mathcal{M} = \frac{(M_1 M_2)^{3/5}}{(M_1+M_2)^{1/5}}$ and $\eta = \frac{M_1 M_2}{(M_1+M_2)^2}$ are the chirp mass and symmetric mass ratio, respectively; R.A. (right ascension) and Dec (declination) identify the source position in the sky; the angles θ_{J_0} and ϕ_{J_0} identify the direction of the total angular momentum; d_L is the luminosity distance to the source; $0 \leq a_{\mathrm{spin}} \equiv S/M_1^2 \leq 1$ is the dimensionless spin magnitude; θ_{SL} is the angle between the spin and the orbital angular momentum; and ϕ_c and α_c are integration phase constants.

We have optimized the MCMC algorithm by including a variety of features to efficiently sample the parameter space, such as parallel tempering [160]. Our MCMC implementation can be run on a data set from a single detector, or on data sets from multiple detectors; in the latter case, a coherent search among all detectors significantly improves the determination of source position and orientation [159, 160].

We ran our MCMC code on a selection of NINJA waveforms. We found that although the MCMC runs are clearly able to detect a signal whenever the inspiral contains a sufficient signal-to-noise ratio (SNR), they were unable to correctly determine the signal parameters for many injections. For the high masses typical of most NINJA injections, the SNR is dominated by the merger and ringdown, so our inspiral-only templates tried to match the merger and ringdown portions of the injected waveform. Typically, we find that in such cases the time of coalescence is overestimated since the injected ringdown is matched to an inspiral; the chirp mass is underestimated since the merger/ringdown frequency is higher than the inspiral frequency for a given mass, so that matching them to an inspiral requires the mass to be lower; the mass ratio is underestimated, which allows the waveform to contain more energy in the narrow frequency band corresponding to quasinormal ringing; and the spin rails against the upper prior of 1.000 since the innermost stable circular orbit frequency is highest for an inspiral into a maximally-spinning Kerr black hole. We tried to circumvent the problem of matching to the merger and ringdown by introducing more restrictive priors on spin and/or η. These efforts still failed when the total masses were too high, but were successful in the case of lower total masses and longer inspiral signals.

Figure 18 shows the PDFs produced by runs on an injected equal-mass non-spinning `SpEC` Cornell/Caltech waveform with $\mathcal{M} = 15.6 M_\odot$. We chose this particular

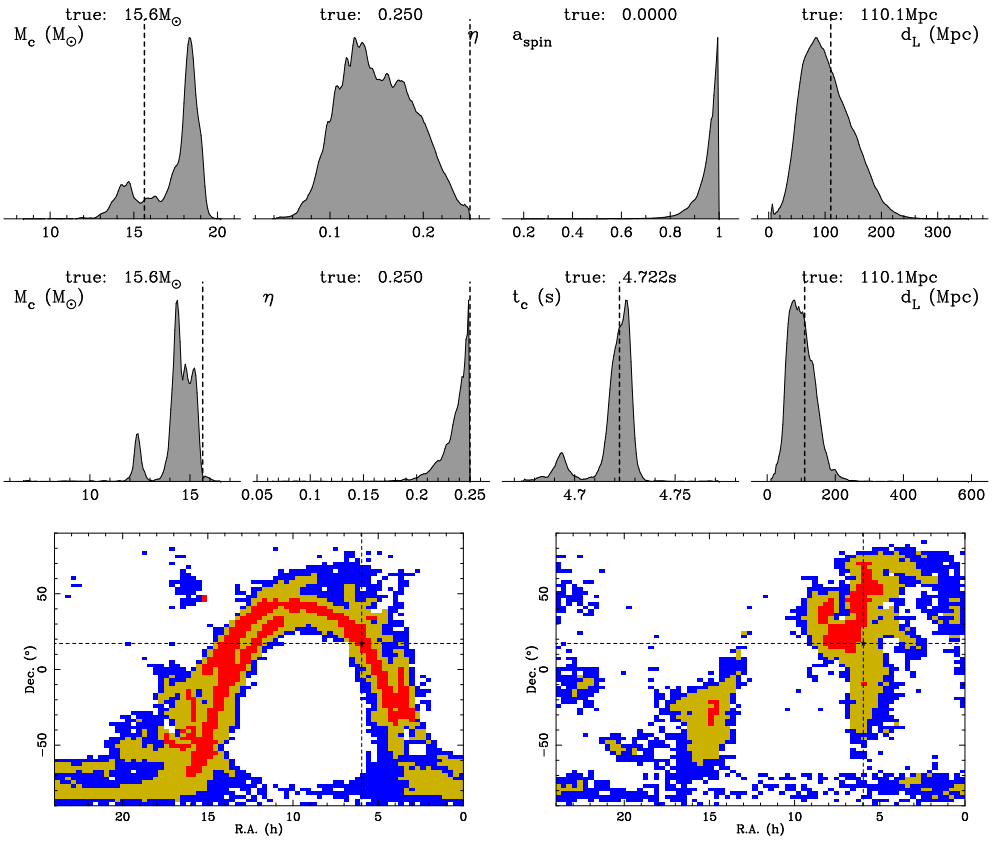

Figure 18. Top row: marginalized PDFs for $\mathcal{M}$, η, a, d_L produced by a 2-detector run on an injected non-spinning equal-mass `SpEC` Cornell/Caltech waveform (true values $\mathcal{M} = 15.6M_\odot$, $\eta = 0.25$, $t_c = \ldots 4.7223$s, and $a = 0$). Middle row: the same PDFs (but with a replaced by t_c) for a 3-detector run with constrained spin on the same injection. Bottom row: two-dimensional PDFs for the sky position with the 2-detector run on the left and the 3-detector run on the right; red is the 1-σ probability area, yellow is the 2-σ area, and blue is the 3-σ area. Dashed lines denote the true values of injected parameters.

injection because it had the lowest total mass, and `SpEC` waveforms typically have more inspiral cycles; runs on other injections show comparable results, with the general trend that the higher the total mass (and, thus, the lower the relative fraction of the SNR contributed by the inspiral), the poorer the parameter estimation becomes.

Data from two detectors, H1 and L1, were used to compute the PDF in the top row of Figure 18. We used wide, flat priors for intrinsic parameters (e.g., $\mathcal{M} \in [2M_\odot, 100M_\odot]$, $\eta \in [0.03, 0.25]$, $a_{\rm spin} \in [0, 1]$). We find that the values of the intrinsic parameters are not determined very accurately. In particular, the spin rails against the upper bound of 1 while η is underestimated, as expected and explained above. We find that the sky location is nevertheless constrained to an arc of a ring containing the true value; the 2-σ ($\sim 95\%$) sky area of the ring shown in the bottom left of Fig. 18 is ~ 10000 square degrees.

In the middle row of Fig. 18, we plot the PDFs based on data from three detectors:

H1, L1, and V1. We constrained the spin parameter to its true value $a_{\rm spin} = 0$ for this run. This had the effect of forcing the MCMC to match the inspiral only, significantly improving the resolution of other parameters: for example, the PDF of η now rails against 0.25, which is its true value. The chirp mass is still somewhat underestimated; a higher SNR may be necessary to improve the mass determination. Promisingly, we find that the sky location is constrained to a smaller patch on the sky: the 2-σ sky area in the bottom right of Fig. 18 is 6300 square degrees. In fact, the sky localization is even better when the spin parameter is set free, allowing the MCMC to use the SNR contributed by the ringdown; removing the spin-parameter constraint reduces the 2-σ sky area to 2750 square degrees. This ability to determine the source position will be significant in any future searches for electromagnetic counterparts of gravitational-wave triggers.

We hope that in the future it will be possible to test our MCMC code on numerical signals in a lower mass range, where the inspiral portion would dominate the SNR, so that our inspiral-only templates are not at a significant disadvantage. Meanwhile, we have recently implemented non-restricted templates at 3.5 PN order in phase and 2.5 PN order in amplitude that will include spins for both members of the binary, thus improving the accuracy of parameter estimation and increasing the range of applicability of our code.

4.4.2. Bayesian Model Selection Pipeline The primary goal was to investigate the performance of different template families on the confidence of detection of the injections contained in the NINJA data set. We tackle this problem using a method described in [162, 163]. In short, this approach can be summarised as follows: two hypotheses are under consideration:

- H_N: The data $\{\tilde{d}_k\}$ are described by (Gaussian and stationary) noise only: $\tilde{d}_k = \tilde{n}_k$
- H_S: The data $\{\tilde{d}_k\}$ are described by (Gaussian and stationary) noise $\{\tilde{n}_k\}$ *and* a gravitational wave signal $\{\tilde{h}_k^{(a)}(\vec{\theta})\}$, according to a given approximant a, where $\vec{\theta}$ represents the vector of the (unknown) signal parameters: $\tilde{d}_k = \tilde{n}_k + \tilde{h}_k^{(a)}(\vec{\theta})$.

The marginal likelihood of H_S, is calculated by performing the integral

$$p(\{\tilde{d}_k\}|H_s, a) = \int p(\vec{\theta}) p(\{\tilde{d}_k\}|H_S, a, \vec{\theta}) d\vec{\theta}, \tag{15}$$

where $p(\vec{\theta})$ is the prior probability density of the parameters $\vec{\theta}$. The ratio of probabilities or "odds ratio" of the two models is

$$\mathcal{O}_{SN,a} = \frac{P(H_S|\{\tilde{d}_k\}, a)}{P(H_N|\{\tilde{d}_k\})} = \left[\frac{P(H_S)}{P(H_N)}\right] \left[\frac{P(\{\tilde{d}_k\}|H_S, a)}{P(\{\tilde{d}_k\}|H_N)}\right] = \mathcal{P}\, B_{SN}^{(a)}, \tag{16}$$

where $\mathcal{P}$ is the *prior odds ratio* and $B_{SN}^{(a)}$ is the *Bayes factor*.

In his analysis we used a model which includes the response of all available interferometers – therefore L1, H1, H2 and V1 – coherently, and the gravitational wave-form is calculated using the LAL library [121]. For the gravitational waveform, we considered two different approximants: the standard (2 PN) TaylorF2 waveform family, with inspiral truncated at $6M$, and the phenomenological inspiral-merger-ringdown IMRPhenA templates described in [143]. In each case we terminated the waveforms at a lower frequency of 30 Hz.

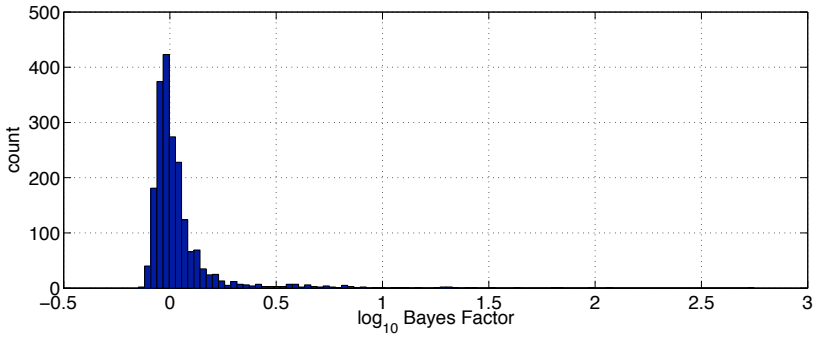

Figure 19. The distribution of Bayes factors obtained by running the algorithm on signal-free data sets. The pipeline was run coherently on the four interferometers, and the same was done for the results reported in this figure. The total number of trials is 2000 and the highest value of the Bayes factor is $\log_{10} B = 2.77$.

The choice of priors in the analysis was as follows.For the TaylorF2 approximant, the prior on $\vec{\theta}$ was uniform on component masses and distance, within the following limits: time of coalescence in a window $\pm 0.5\,\mathrm{s}$ around the actual t_c of each injection, total mass in the range $50M_\odot \leq M \leq 150M_\odot$, symmetric mass ratio η in the range $0.01 \leq \eta \leq 0.25$, and distance $1 \leq D \leq 500$ Mpc. The parameters for orientation and position on the sky of the binary were allowed to vary over their entire angular ranges. For the IMRPhenA approximant, the limits were identical on all the parameters, with the exception of the total mass whose upper boundary was set to $475M_\odot$. We also calculated the Bayes factors for data segments containing no signal in order to estimate the background distribution of Bayes factors. Figure 19 shows the distribution of Bayes factors (using TaylorF2 approximants) when running the analysis algorithm on portions of data without injections: 2000 trials were carried out, with a maximum value of $\log_{10} B = 2.77$. If interpreted as a threshold value on the Bayes factors to decide whether a signal and been detected or not, it corresponds to a false alarm of 0.05%. The distribution obtained with the IMRPhenA approximant is very similar. In the analysis we considered a range of "detection thresholds" on $\log_{10} B$, in order to explore how the two different approximants (and the algorithm) respond to different numerical relativity injections.

Figure 20 and Table 9 summarise the main results. The left panel of Figure 20 shows the value of the Bayes factor computed for the two approximants as a function of the coherent 4-interferometer signal-to-noise ratio at which the waveforms were injected. For *all* the injections, IMRPhenA approximants return a Bayes factor which is (significantly) larger than TaylorF2 approximants. This is not surprising, as the TaylorF2 waveforms do not contain the merger and ring-down portion of the coalescence. Figure 20 (right panel) shows the number of injections that are recovered at a given Bayes factor (or above). Once more the effectiveness of IMRPhenA approximants is striking compared to the TaylorF2 waveform family.

The nested-sampling algorithm used for model-selection can also be used for parameter estimation. In particular, one can generate in a straightforward way the maximum likelihood estimate of the recovered parameters, and have an indication of the statistical errors on such values. For simplicity, in this analysis we identified the

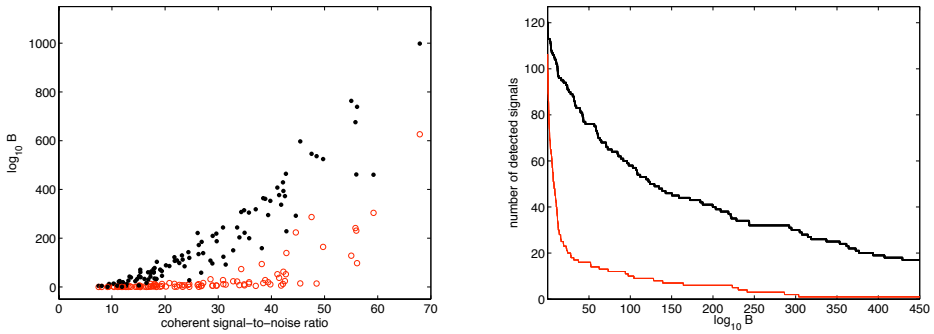

Figure 20. Left: The values of the Bayes factors obtained in the analysis of the NINJA data set as a function of the optimal coherent (L1-H1-H2-V1) signal-to-noise ratio at which the signals were injected into instrument noise. The solid (black) dots and the open (red) circles refer to the Bayes factors obtained by using the IMRPhenA and TaylorF2 approximants, respectively. Right: The cumulative number of injections recovered as a function of the Bayes factor. The thin (red) solid line corresponds to the results obtained by using the TaylorF2 approximant, whereas the think (black) solid line refers to the IMRPhenA approximant. A threshold $\log_{10} B_{SN} = 3$ has been used.

Threshold	Number of detected injections	
($\log_{10} B$)	TaylorF2	IMRPhenA
3	69	112
5	61	107
10	43	104
30	28	89
100	10	58

Table 9. Results of the analysis of the NINJA data using TaylorF2 and IMRPhenA approximant with the model-selection pipeline using different thresholds in Bayes factor. The total number of injections was 126. See also Figure 20.

statistical errors (the error bars in Figures 21 and 22) with the region of parameter space in which the likelihood values were not lower than a factor e with respect to the maximum likelihood. The results for chirp mass, total mass and the two co-oordinates of the source in the sky – latitude and longitude – are shown in Figures 21 and 22; here we restrict to only the IMRPhenA approximant and to all the signals that yielded $\log_{10} B \geq 3$. The results for the masses show a behaviour that is consistent to what shown in previous sections. The total mass is (in most of the cases) systematically underestimated, although for 33 injections the recovered values were consistent with the injected total mass. We have also checked that the errors on the masses do not show any significant correlation with the value of the Bayes factor at which the injections were recovered or the injected signal-to-noise ratio. However, despite the systematic errors on the physical parameters, the sky location is on average fairly well determined. This is most likely due to the fact that there is enough information in the (source location dependent) time of arrival of the signals at different instrument sites to recover meaningful information about the position of the source in the celestial sphere. This is currently under more careful investigation.

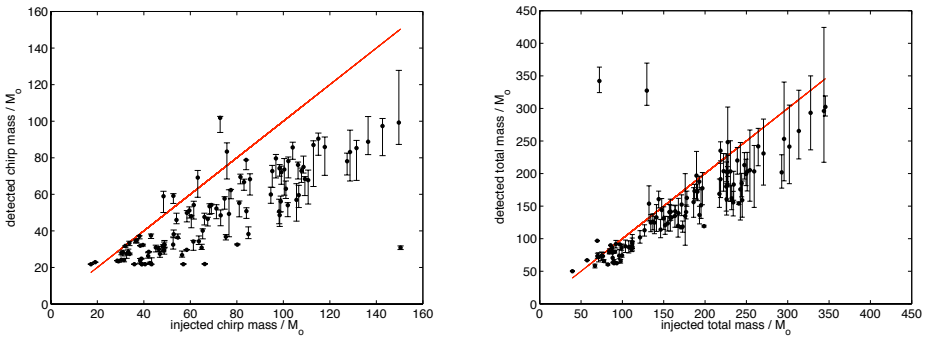

Figure 21. Left: The recovered (maximum likelihood) values of the chirp mass as a function of the injected values. Right: The recovered (maximum likelihood) values of the total mass as a function of the injected values.

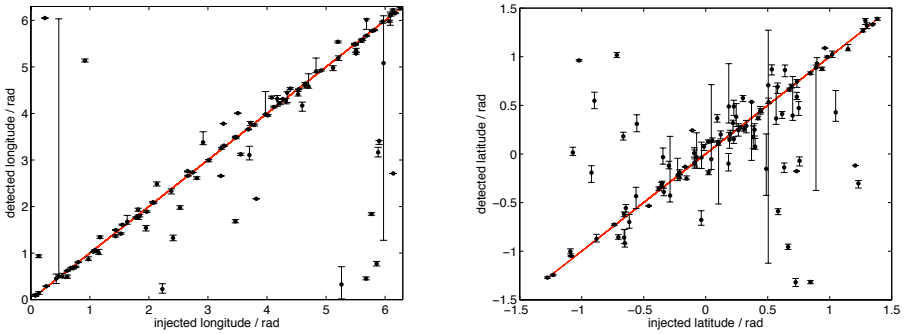

Figure 22. Left: The recovered (maximum likelihood) values of the source longitude as a function of the injected values. Right: The recovered (maximum likelihood) values of the source latitude as a function of the injected values.

5. Discussion[Needs volunteer]

We have presented the results of the first NINJA analysis. This project was conceived as a first step towards a long term collaboration between numerical relativists and data analysts in an attempt to use numerical waveforms to enhance searches for gravitational waves. The work is unique in that it focused on running existing gravitational wave search algorithms on data containing waveforms obtained from numerical simulations.

The project began with the submission of numerical gravitational waveforms from merging black holes produced from several different numerical codes. These waveforms were used to construct astrophysically realisitic GW signals of given masses and sky location which were embedded into simulated data at the design sensitivity of the initial LIGO and Virgo instruments. Finally, various data analysis methods were employed in an effort to extract the parameters of the waveforms from the noisy data. Since it was the first such analysis, the scope of the project was deliberately kept somewhat modest, with a restriction on the number of waveforms to be submitted by each numerical group and only a limited number of simulated signals produced for the

data analysis. This helped to encourage significant involvement from both numerical relativity and data analysis groups, with ten numerical relativity groups providing waveforms and also ten different data analysis contributions.

Communication between the data analysis and numerical communities has been relatively smooth, with the data format outlined in [54] providing a good first specification of the numerical data format. During the course of the project, a few potential refinements and improvements were identified .... Doubtless, the format will require additional modification as more complex waveforms are generated and once the project is extended to include waveforms from sources other than BBHs. For example, supernovae or binary neutron star inspiral waveforms do not have the same overall mass scaling as black hole waveforms, so clearly will require an extra parameter.

The limited number of both waveforms submitted make it dangerous to draw strong conclusions from the comparison of different waveform families and different search methods. Overall, it is clear that many of the data analysis methods were capable of detecting a significant fraction of the simulated waveforms. This is immediately significant as several of the analyses performed are routinely used in searches of the LIGO and Virgo data, thus providing reassurance that standard analysis techniques are indeed sensitive to the *full* (I do not think we can quite conclude this - since only a limited number of spinning waveforms were submitted and many waveforms were pretty short in duraction - DS) compact binary coalescence gravitational waveform. For parameter estimation, the results are less clear cut, with several methods tending to associate a candidate event to that part of the waveform which lies in the most sensitive band of the detector. For example, in a search with inspiral only templates, the ringdown of a high mass black hole which occurs at around 100 Hz might be picked up. This will lead to poor estimation of both the binary's mass and coalescence time. Similarly, the unmodelled burst searches will correctly identify the signal but, without knowing which part of the coalescence it corresponds to, have difficulty providing accurate parameters. There is some evidence that using full inspiral-merger-ringdown waveform templates alleviates this problem, as well as evidence that estimation of the sky location of the signal is largely independent of the mismatches between simulated and template waveform. These are all issues which warrant further investigation.

In the future, we hope to continue and extend the NINJA work. Several suggestions have been made to both broaden the work and make it more systematic. To extend the effort, it would be natural to branch out into other waveform families, such as supernovae or binary mergers comprising at least one neutron star. Several groups have requested a signal free data set which could be used in testing and tuning of various parameters in the search algorithms. Others have suggested that we release both training and challenge data sets, in a manner similar to the Mock LISA Data Challenges. Whatever is decided, it is clear that there is plenty more to be learned from collaborations between numerical relativists and data analysts.

Acknowledgements

We thank the Kavli Institute for Theoretical Physics (KITP) Santa Barbara for hospitality during the workshop "Interplay between Numerical Relativity and Data Analysis", where the NINJA project was initiated; the Kavli Institute is supported by NSF grant PHY 05-51164.

FP gratefully acknowledges support from the Alfred P. Sloan Foundation and NSF PHY-0745779. Work supported by NSF grants PHY-0653443 (DS), PHY-055436 (PL), PHY-0653303 (PL, DS), PY-0114375 (CGWP), PHY-0354842 (RM), PHY-0652874 (FAU), NASA NNG-04GL37G (RM) and the computations were carried out under LRAC allocations MCA08X009 (PL, DS), TG-MCA08X010 (FAU), TG-MCA02N014 (LSU). PB, LG, AM, RV acknowledge support from the National Science Foundation awards PHY-0701817 and PHY-0600953.

This work is partially supported by NSF Gravitational Physics Grant (PHY-0353111) to VK and PHY-0653550 to LC. NC was supported by NSF grant PHY-0553422.

BA was supported by a Vacation Bursary of the UK Engineering and Physical Sciences Research Council. AV and JV acknowledge support by the UK Science and Technology Facilities Council.

BS acknowledges the support of the UK Science and Technology Facilities Council. SF was funded by the Royal Society. BF was funded by the International REU program and grant NSF-0838740.

References

[1] Thorne K S 1987 *Three hundred years of gravitation* ed Hawking S W and Israel W (Cambridge: Cambridge University Press) chap 9, pp 330–458
[2] Einstein A 1916 *Preuss. Akad. Weiss. Berlin* 688
[3] Peters P C and Mathews J 1963 *Phys. Rev.* **131** 435–439
[4] Peters P C 1964 *Phys. Rev.* **136** B1224–B1232
[5] Barish B C and Weiss R 1999 *Phys. Today* **52N10** 44–50
[6] Acernese F *et al.* (VIRGO) 2005 *AIP Conf. Proc.* **794** 307–310
[7] Tsubono K (TAMA) 2000 Prepared for 9th Marcel Grossmann Meeting on Recent Developments in Theoretical and Experimental General Relativity, Gravitation and Relativistic Field Theories (MG 9), Rome, Italy, 2-9 Jul 2000
[8] Willke B (LIGO Scientific) 2007 *Class. Quant. Grav.* **24** S389–S397
[9] Abbott B *et al.* (LIGO Scientific) 2004 *Nucl. Instrum. Meth.* **A517** 154–179 (*Preprint* gr-qc/0308043)
[10] Abbott B *et al.* (LIGO Scientific) 2007 (*Preprint* 0711.3041)
[11] Acernese F *et al.* 2008 *J. Phys. Conf. Ser.* **120** 032007
[12] Abbott B *et al.* (LIGO Scientific) 2004 *Phys. Rev. D* **69** 122001 (*Preprint* gr-qc/0308069)
[13] Abbott B *et al.* (LIGO Scientific) 2005 *Phys. Rev.* **D72** 082001 (*Preprint* gr-qc/0505041)
[14] Abbott B *et al.* (LIGO Scientific) 2005 *Phys. Rev.* **D72** 082002 (*Preprint* gr-qc/0505042)
[15] Abbott B *et al.* (LIGO Scientific) 2008 *Phys. Rev. D* **77** 062002 (*Preprint* 0704.3368)
[16] Abbott B *et al.* (LIGO Scientific) 2008 *Phys. Rev.* **D78** 042002 (*Preprint* 0712.2050)
[17] Abbott B *et al.* (LIGO) 2004 *Phys. Rev.* **D69** 102001 (*Preprint* gr-qc/0312056)
[18] Abbott B *et al.* (LIGO Scientific) 2005 *Phys. Rev.* **D72** 062001 (*Preprint* gr-qc/0505029)
[19] Abbott B *et al.* (LIGO Scientific) 2006 *Class. Quant. Grav.* **23** S29–S39 (*Preprint* gr-qc/0511146)
[20] Abbott B *et al.* (TAMA) 2005 *Phys. Rev.* **D72** 122004 (*Preprint* gr-qc/0507081)
[21] Abbott B *et al.* (LIGO Scientific) 2007 *Class. Quant. Grav.* **24** 5343–5370 (*Preprint* 0704.0943)
[22] Pretorius F 2005 *Phys. Rev. Lett.* **95** 121101 (*Preprint* gr-qc/0507014)
[23] Campanelli M, Lousto C O, Marronetti P and Zlochower Y 2006 *Phys. Rev. Lett.* **96** 111101 (*Preprint* gr-qc/0511048)
[24] Baker J G, Centrella J, Choi D I, Koppitz M and van Meter J 2006 *Phys. Rev. Lett.* **96** 111102 (*Preprint* gr-qc/0511103)
[25] Herrmann F, Hinder I, Shoemaker D and Laguna P 2007 *Class. Quant. Grav.* **24** S33–S42
[26] Baker J G *et al.* 2006 *Astrophys. J.* **653** L93–L96 (*Preprint* astro-ph/0603204)
[27] Herrmann F, Hinder I, Shoemaker D, Laguna P and Matzner R A 2007 *Astrophys. J.* **661** 430–436 (*Preprint* gr-qc/0701143)
[28] Koppitz M *et al.* 2007 *Phys. Rev. Lett.* **99** 041102 (*Preprint* gr-qc/0701163)
[29] Campanelli M, Lousto C O, Zlochower Y and Merritt D 2007 *Astrophys. J.* **659** L5–L8 (*Preprint* gr-qc/0701164)

[30] Gonzalez J A, Hannam M D, Sperhake U, Bruegmann B and Husa S 2007 *Phys. Rev. Lett.* **98** 231101 (*Preprint* gr-qc/0702052)
[31] Campanelli M, Lousto C O, Zlochower Y and Merritt D 2007 *Phys. Rev. Lett.* **98** 231102 (*Preprint* gr-qc/0702133)
[32] Baker J G *et al.* 2007 *Astrophys. J.* **668** 1140–1144 astro-ph/0702390
[33] Herrmann F, Hinder I, Shoemaker D M, Laguna P and Matzner R A 2007 *Phys. Rev.* **D76** 084032 (*Preprint* 0706.2541)
[34] Bruegmann B, Gonzalez J A, Hannam M, Husa S and Sperhake U 2008 *Phys. Rev. D* **77** 124047 (*Preprint* 0707.0135)
[35] Schnittman J D *et al.* 2008 *Phys. Rev.* **D77** 044031 (*Preprint* 0707.0301)
[36] Pollney D *et al.* 2007 *Phys. Rev. D* **76** 124002 (*Preprint* 0707.2559)
[37] Lousto C O and Zlochower Y 2008 *Phys. Rev.* **D77** 044028 (*Preprint* 0708.4048)
[38] Baker J G *et al.* 2008 *Astrophys. J.* **682** L29 (*Preprint* 0802.0416)
[39] Dain S, Lousto C O and Zlochower Y 2008 *Phys. Rev.* **D78** 024039 (*Preprint* 0803.0351)
[40] Healy J *et al.* 2008 (*Preprint* 0807.3292)
[41] Gonzalez J A, Sperhake U and Bruegmann B 2008 (*Preprint* 0811.3952)
[42] Campanelli M, Lousto C O and Zlochower Y 2006 *Phys. Rev.* **D74** 084023 (*Preprint* astro-ph/0608275)
[43] Gonzalez J A, Sperhake U, Bruegmann B, Hannam M and Husa S 2007 *Phys. Rev. Lett.* **98** 091101
[44] Campanelli M, Lousto C O, Zlochower Y, Krishnan B and Merritt D 2007 *Phys. Rev.* **D75** 064030 (*Preprint* gr-qc/0612076)
[45] Rezzolla L *et al.* 2008 *Astrophys.* **J679** 1422–1426 (*Preprint* 0708.3999)
[46] Boyle L, Kesden M and Nissanke S 2008 *Phys. Rev. Lett.* **100** 151101 (*Preprint* 0709.0299)
[47] Rezzolla L *et al.* 2008 *Astrophys. J.* **674** L29–L32 (*Preprint* 0710.3345)
[48] Marronetti P, Tichy W, Bruegmann B, Gonzalez J and Sperhake U 2008 *Phys. Rev.* **D77** 064010 (*Preprint* 0709.2160)
[49] Sperhake U *et al.* 2008 *Phys. Rev.* **D78** 064069 (*Preprint* 0710.3823)
[50] Hinder I, Vaishnav B, Herrmann F, Shoemaker D and Laguna P 2008 *Phys. Rev. D* **77** 081502 (*Preprint* 0710.5167)
[51] Boyle L and Kesden M 2008 *Phys. Rev.* **D78** 024017 (*Preprint* 0712.2819)
[52] Tichy W and Marronetti P 2008 *Phys. Rev. D* **78** 081501 (*Preprint* 0807.2985)
[53] Rezzolla L 2008 (*Preprint* 0812.2325)
[54] Brown D A *et al.* 2007 Data formats for numerical relativity waves (*Preprint* 0709.0093)
[55] Hannam M, Husa S, Sperhake U, Bruegmann B and Gonzalez J A 2008 *Phys. Rev. D* **77** 044020 (*Preprint* 0706.1305)
[56] Husa S, Hannam M, Gonzalez J A, Sperhake U and Bruegmann B 2008 *Phys. Rev. D* **77** 044037 (*Preprint* 0706.0904)
[57] Bruegmann B *et al.* 2008 *Phys. Rev. D* **77** 024027 (*Preprint* gr-qc/0610128)
[58] Husa S, Gonzalez J A, Hannam M, Bruegmann B and Sperhake U 2008 *Class. Quant. Grav.* **25** 105006 (*Preprint* 0706.0740)
[59] Hannam M, Husa S, Bruegmann B and Gopakumar A 2008 *Phys. Rev. D* **78** 104007 (*Preprint* 0712.3787)
[60] Alcubierre M *et al.* 2000 *Phys. Rev.* **D62** 044034 (*Preprint* gr-qc/0003071)
[61] Alcubierre M *et al.* 2003 *Phys. Rev. D* **67** 084023 (*Preprint* gr-qc/0206072)
[62] Kidder L E 1995 *Phys. Rev. D* **52** 821–847 (*Preprint* gr-qc/9506022)
[63] Imbiriba B *et al.* 2004 *Phys. Rev. D* **70** 124025 (*Preprint* gr-qc/0403048)
[64] van Meter J R, Baker J G, Koppitz M and Choi D I 2006 *Phys. Rev. D* **73** 124011 (*Preprint* gr-qc/0605030)
[65] Zlochower Y, Baker J G, Campanelli M and Lousto C O 2005 *Phys. Rev. D* **72** 024021 (*Preprint* gr-qc/0505055)
[66] Sperhake U 2007 *Phys. Rev. D* **76** 104015 (*Preprint* gr-qc/0606079)
[67] Vaishnav B, Hinder I, Herrmann F and Shoemaker D 2007 *Phys. Rev. D* **76** 084020 (*Preprint* 0705.3829)
[68] Pretorius F 2005 *Class. Quant. Grav.* **22** 425–452 (*Preprint* gr-qc/0407110)
[69] Buonanno A, Cook G B and Pretorius F 2007 *Phys. Rev. D* **75** 124018 (*Preprint* gr-qc/0610122)
[70] Cook G B and Pfeiffer H P 2004 *Phys. Rev. D* **70** 104016 (*Preprint* gr-qc/0407078)
[71] Pretorius F and Khurana D 2007 *Class. Quant. Grav.* **24** S83–S108 (*Preprint* gr-qc/0702084)
[72] Scheel M A *et al.* 2006 *Phys. Rev. D* **74** 104006 (*Preprint* gr-qc/0607056)
[73] Boyle M *et al.* 2007 *Phys. Rev. D* **76** 124038 (*Preprint* 0710.0158)

[74] Scheel M A *et al.* 2008 High-accuracy waveforms for binary black hole inspiral, merger, and ringdown (*Preprint* 0810.1767)
[75] Pfeiffer H P *et al.* 2007 *Class. Quant. Grav.* **24** S59–S82 (*Preprint* gr-qc/0702106)
[76] Etienne Z B, Faber J A, Liu Y T, Shapiro S L and Baumgarte T W 2007 *Phys. Rev. D* **76** 101503 (*Preprint* 0707.2083)
[77] Tichy W and Bruegmann B 2004 *Phys. Rev. D* **69** 024006 (*Preprint* gr-qc/0307027)
[78] Bowen J M and York James W J 1980 *Phys. Rev. D* **21** 2047–2056
[79] Beig R and Murchadha N O 1994 *Class. Quant. Grav.* **11** 419–430 (*Preprint* gr-qc/9304034)
[80] Brandt S and Bruegmann B 1997 *Phys. Rev. Lett.* **78** 3606–3609 (*Preprint* gr-qc/9703066)
[81] Dain S and Friedrich H 2001 *Commun. Math. Phys.* **222** 569–609 (*Preprint* gr-qc/0102047)
[82] Thornburg J *et al.* 2007 *Class. Quant. Grav.* **24** 3911–3918 (*Preprint* gr-qc/0701038)
[83] Ansorg M, Bruegmann B and Tichy W 2004 *Phys. Rev. D* **70** 064011 (*Preprint* gr-qc/0404056)
[84] http://www.lorene.obspm.fr/
[85] Brown J D and Lowe L L 2005 *J. Comput. Phys.* **209** 582–598 (*Preprint* gr-qc/0411112)
[86] York James W J 1999 *Phys. Rev. Lett.* **82** 1350–1353 (*Preprint* gr-qc/9810051)
[87] Caudill M, Cook G B, Grigsby J D and Pfeiffer H P 2006 *Phys. Rev. D* **74** 064011 (*Preprint* gr-qc/0605053)
[88] Christodoulou D 1970 *Phys. Rev. Lett.* **25** 1596–1597
[89] Cook-pfeiffer initial data URL http://www.black-holes.org/~harald/PublicID/Nonspinning/BBH_QuasiEquilibrium_Nonspinning_59a_10.00.tgz
[90] Konigsdorffer C and Gopakumar A 2006 *Phys. Rev. D* **73** 124012 (*Preprint* gr-qc/0603056)
[91] York Jr J W 1979 *Sources of Gravitational Radiation* ed Smarr L (Cambridge University Press, Cambridge) pp 83–126
[92] Wald R M 1984 *General relativity* (Chicago: The University of Chicago Press) ISBN 0-226-87032-4 (hardcover), 0-226-87033-2 (paperback)
[93] Friedrich H and Rendall A D 2000 *Lect. Notes Phys.* **540** 127–224 (*Preprint* gr-qc/0002074)
[94] Lindblom L, Scheel M A, Kidder L E, Owen R and Rinne O 2006 *Class. Quant. Grav.* **23** S447–S462 (*Preprint* gr-qc/0512093)
[95] Pretorius F 2006 *Class. Quantum Grav.* **23** S529–S552 (*Preprint* gr-qc/0602115)
[96] Nakamura T, Oohara K and Kojima Y 1987 *Prog. Theor. Phys. Suppl.* **90** 1–218
[97] Shibata M and Nakamura T 1995 *Phys. Rev. D* **52** 5428–5444
[98] Baumgarte T W and Shapiro S L 1999 *Phys. Rev. D* **59** 024007 (*Preprint* gr-qc/9810065)
[99] Bona C, Masso J, Seidel E and Stela J 1997 *Phys. Rev. D* **56** 3405–3415 (*Preprint* gr-qc/9709016)
[100] Hannam M, Husa S, Pollney D, Bruegmann B and O'Murchadha N 2007 *Phys. Rev. Lett.* **99** 241102 (*Preprint* gr-qc/0606099)
[101] Hannam M *et al.* 2007 *J. Phys. Conf. Ser.* **66** 012047 (*Preprint* gr-qc/0612097)
[102] Hannam M, Husa S, Ohme F, Bruegmann B and O'Murchadha N 2008 *Phys. Rev. D* **78** 064020 (*Preprint* 0804.0628)
[103] Baker J G, Centrella J, Choi D I, Koppitz M and van Meter J 2006 *Phys. Rev. D* **73** 104002 (*Preprint* gr-qc/0602026)
[104] Gundlach C and Martin-Garcia J M 2006 *Phys. Rev. D* **74** 024016 (*Preprint* gr-qc/0604035)
[105] Moncrief V 1974 *Ann. Phys.* **88** 323–342
[106] Nagar A and Rezzolla L 2005 *Class. Quant. Grav.* **22** R167 (*Preprint* gr-qc/0502064)
[107] Nagar A and Rezzolla L 2005 *Class. Quantum Grav.* **22** R167–R192 erratum-ibid. **23**, 4297, (2006)
[108] Sarbach O and Tiglio M 2001 *Phys. Rev. D* **64** 084016 (*Preprint* gr-qc/0104061)
[109] Baker J G, Campanelli M and Lousto C O 2002 *Phys. Rev. D* **65** 044001 (*Preprint* gr-qc/0104063)
[110] Damour T, Nagar A, Hannam M, Husa S and Bruegmann B 2008 *Phys. Rev. D* **78** 044039 (*Preprint* 0803.3162)
[111] Baker J G and van Meter J R 2005 *Phys. Rev. D* **72** 104010 (*Preprint* gr-qc/0505100)
[112] Kreiss H O and Oliger J 1973 *Methods for the approximate solution of time dependent problems* (Geneva: GARP publication series No. 10)
[113] Gustafsson B, Kreiss H O and Oliger J 1995 *Time dependent problems and difference methods* (New York: Wiley)
[114] Goodale T, Allen G, Lanfermann G, Massó J, Radke T, Seidel E and Shalf J 2003 *Vector and Parallel Processing – VECPAR'2002, 5th International Conference, Lecture Notes in Computer Science* (Berlin: Springer)
[115] Cactus computational toolkit URL http://www.cactuscode.org/
[116] Schnetter E, Hawley S H and Hawke I 2004 *Class. Quant. Grav.* **21** 1465–1488 (*Preprint*

gr-qc/0310042)
[117] Schnetter E Carpet: A mesh refinement driver for cactus URL http://www.carpetcode.org/
[118] MacNeice P, Olson K, Mobarry C, de Fainchtein R and Packer C 2000 *Comput. Phys. Commun.* **126** 330–354
[119] Rinne O, Lindblom L and Scheel M A 2007 *Class. Quant. Grav.* **24** 4053–4078 (*Preprint* 0704.0782)
[120] Thornburg J 2004 *Class. Quant. Grav.* **21** 743–766 (*Preprint* gr-qc/0306056)
[121] Lsc algorithm library URL http://www.lsc-group.phys.uwm.edu/lal
[122] Wainstein L A and Zubakov V D 1962 *Extraction of signals from noise* (Englewood Cliffs, NJ: Prentice-Hall)
[123] Helmstrom C W 1968 *Statistical Theory of Signal Detection* (London: Permagon)
[124] The LIGO Scientific Collaboration 2007 Tuning matched filter searches for compact binary coalescence Tech. Rep. LIGO-T070109-01 LIGO Project URL http://www.ligo.caltech.edu/docs/T/T070109-01.pdf
[125] Owen B J and Sathyaprakash B S 1999 *Phys. Rev. D* **60** 022002 (*Preprint* gr-qc/9808076)
[126] Babak S, Balasubramanian R, Churches D, Cokelaer T and Sathyaprakash B S 2006 *Class. Quant. Grav.* **23** 5477–5504 (*Preprint* gr-qc/0604037)
[127] Cokelaer T 2007 *Phys. Rev. D* **76** 102004 (*Preprint* 0706.4437)
[128] Creighton J D E 1999 *Phys. Rev. D* **60** 022001 (*Preprint* gr-qc/9901084)
[129] Allen B, Anderson W G, Brady P R, Brown D A and Creighton J D E 2005 FINDCHIRP: An algorithm for detection of gravitational waves from inspiraling compact binaries (*Preprint* gr-qc/0509116)
[130] Robinson C A K, Sathyaprakash B S and Sengupta A S 2008 A geometric algorithm for efficient coincident detection of gravitational waves (*Preprint* 0804.4816)
[131] Goggin L M 2008 *A search for gravitational waves from perturbed black hole ringdowns in LIGO data* Ph.D. thesis Caltech
[132] Allen B 2005 *Phys. Rev. D* **71** 062001 (*Preprint* gr-qc/0405045)
[133] Rodríguez A 2007 *Reducing false alarms in searches for gravitational waves from coalescing binary systems* Master's thesis Louisiana State University URL http://www.ligo.caltech.edu/docs/P/P070056-00.pdf
[134] Droz S, Knapp D J, Poisson E and Owen B J 1999 *Phys. Rev. D* **59** 124016 (*Preprint* gr-qc/9901076)
[135] Abbott B *et al.* (LIGO Scientific) 2008 Search for gravitational waves from low-mass binary coalescences in the first calendar year of s5 ligo data in preparation
[136] Blanchet L 2002 *Living Rev. Rel.* **5** 3 (*Preprint* gr-qc/0202016)
[137] Pan Y *et al.* 2008 *Phys. Rev. D* **77** 024014 (*Preprint* 0704.1964)
[138] Michael Boyle D A B and Pekowsky L 2008 High-accuracy numerical simulations of black-hole binaries: The detection efficiency of post-newtonian template waveforms for black-hole binary searches in ground-based gravitational-wave detectors in preparation
[139] Boyle M *et al.* 2008 High-accuracy numerical simulation of black-hole binaries: Computation of the gravitational-wave energy flux and comparisons with post-Newtonian approximants (*Preprint* 0804.4184)
[140] Baker J G, van Meter J R, McWilliams S T, Centrella J and Kelly B J 2007 *Phys. Rev. Lett.* **99** 181101 (*Preprint* gr-qc/0612024)
[141] Buonanno A and Damour T 1999 *Phys. Rev. D* **59** 084006 (*Preprint* gr-qc/9811091)
[142] Buonanno A and Damour T 2000 Binary black holes coalescence: Transition from adiabatic inspiral to plunge (*Preprint* gr-qc/0011052)
[143] Ajith P *et al.* 2008 *Phys. Rev. D* **77** 104017 (*Preprint* 0710.2335)
[144] Ajith P *et al.* 2007 *Class. Quant. Grav.* **24** S689–S700 (*Preprint* 0704.3764)
[145] Buonanno A *et al.* 2007 *Phys. Rev. D* **76** 104049 (*Preprint* 0706.3732)
[146] Damour T and Nagar A 2008 *Phys. Rev. D* **77** 024043 (*Preprint* 0711.2628)
[147] Damour T, Nagar A, Dorband E N, Pollney D and Rezzolla L 2008 *Phys. Rev. D* **77** 084017 (*Preprint* 0712.3003)
[148] Rezzolla L *et al.* 2008 *Phys. Rev. D* **78** 044002 (*Preprint* 0712.3541)
[149] Echeverria F 1989 *Phys. Rev. D* **40** 3194–3203
[150] Leaver E W 1985 *Proc. Roy. Soc. Lond.* **A402** 285–298
[151] Chatterji S K 2005 *The search for gravitational-wave bursts in data from the second LIGO science run* Ph.D. thesis MIT
[152] Chatterji S, Blackburn L, Martin G and Katsavounidis E 2004 *Class. Quant. Grav.* **21** S1809–S1818 (*Preprint* gr-qc/0412119)
[153] Huang N E, Shen Z, R L S, Wu M C, Shih E H and Zheng Q 1998 *Proc. R. Soc. A* **454** 903

[154] Camp J B, Cannizzo J K and Numata K 2007 *Phys. Rev. D* **75** 061101 (*Preprint* gr-qc/0701148)
[155] Stroeer A, Camp J, Cannizzo J and Gagarin N 2008 in preparation
[156] McNabb J W C *et al.* 2004 *Class. Quant. Grav.* **21** S1705–S1710 (*Preprint* gr-qc/0404123)
[157] Stroeer A and Camp J 2008 nRDA proceedings, in preparation, to appear in same volume
[158] Skilling J 2004 *24th International Workshop on Bayesian Inference and Maximum Entropy Methods in Science and Engineering* (AIP, New York) pp 395–405
[159] van der Sluys M V *et al.* 2008 *ApJ* **688** L61–L65 (*Preprint* 0710.1897)
[160] van der Sluys M *et al.* 2008 *Class. Quant. Grav.* **25** 184011 (*Preprint* 0805.1689)
[161] Apostolatos T A, Cutler C, Sussman G J and Thorne K S 1994 *Phys. Rev. D* **49** 6274–6297
[162] Veitch J and Vecchio A 2008 *Phys. Rev. D* **78** 022001 (*Preprint* 0801.4313)
[163] Veitch J and Vecchio A 2008 *Class. Quant. Grav.* **25** 184010 (*Preprint* 0807.4483)